

THE FLORIDA STATE UNIVERSITY

COLLEGE OF ARTS AND SCIENCES

DEVELOPMENT OF THE COAMPS ADJOINT MESOSCALE MODELING  
SYSTEM FOR ASSIMILATING MICROWAVE RADIANCES WITHIN  
HURRICANES.

By

CLARK MATTHEW AMERAULT

A Dissertation submitted to the  
Department of Meteorology  
in partial fulfillment of the  
requirements for the degree of  
Doctor of Philosophy

Degree Awarded:  
Spring Semester, 2005

The members of the committee approve the dissertation of Clark Matthew Amerault defended on March 29, 2005.

Xiaolei Zou  
Professor Directing Dissertation

Ionel Michael Navon  
Outside Committee Member

James J. O'Brien  
Committee Member

Guosheng Liu  
Committee Member

T.N. Krishnamurti  
Committee Member

The Office of Graduate Studies has verified and approved the above named committee members.

## ACKNOWLEDGEMENTS

I would like to thank my advisor Dr. Zou, who provided me the opportunity to work on an advanced data assimilation research project. She gave me a great deal of responsibility and freedom with this research which allowed me to learn the intricacies of developing a modeling system and assimilating an indirect observation. I am indebted to my committee members (Dr. Liu, Dr. O'Brien, Dr. Navon, and Dr. Krishnamurti) for all the knowledge they have imparted on me both inside and outside the classroom. Dr. Liu was especially helpful in providing me with the radiative transfer codes used in this work. I am grateful for the work of Mr. Zhen Yang and Dr. Qiang Zhao who contributed to the development of the tangent linear and adjoint codes. Jeff Hawkins of the Naval Research Laboratory was extremely helpful in providing the SSM/I observations used in this study. Finally, I would like to thank the members of Dr. Zou's lab for the many times they were able to assist me with different areas of this research.

This work was supported by the Office of Naval Research under grant N00014-01-1-0375. Jeff Hawkins of the Naval Research Laboratory provided the SSM/I observations. This work was partially supported by the FSU School for Computational Science, by a grant of resources on the IBM pSeries 690 Power3-based supercomputer "Teragold." Computer resources were also made available on the Naval Research Laboratory's 128 processor SGI.

## TABLE OF CONTENTS

List of Tables .....	vi
List of Figures .....	vii
Abstract .....	x
<b>1. INTRODUCTION .....</b>	<b>1</b>
<b>2. COAMPS ADJOINT MODELING SYSTEM .....</b>	<b>5</b>
2.1 COAMPS Nonlinear Model .....	5
2.1.1 Governing Equations .....	5
2.1.2 Parameterizations .....	6
2.1.3 Parallel Processing .....	8
2.1.4 Analysis Scheme .....	8
2.2 Tangent Linear and Adjoint Models .....	8
2.2.1 Automatic Adjoint Generation .....	10
2.2.2 Discontinuities .....	10
2.3 Variational Data Assimilation .....	11
2.3.1 4D-Var Formulation .....	11
2.3.2 Minimization .....	12
2.3.3 Preconditioning .....	14
<b>3. TESTS OF THE COAMPS ADJOINT MODEL .....</b>	<b>17</b>
3.1 Testing the Tangent Linear Model .....	17
3.2 Testing the Adjoint Model .....	19
3.3 Gradient Check .....	21
3.4 Twin Experiment .....	22
<b>4. RTM PERFORMANCE AND BACKGROUND ERROR COVARIANCE ESTIMATES OF HYDROMETEOR VARIABLES .....</b>	<b>30</b>
4.1 MM5 .....	30
4.2 Microwave Radiance Observations .....	31
4.3 BDA .....	32
4.4 Radiative Transfer Model .....	33
4.5 Probability Density Functions .....	36
4.6 Error Estimations .....	39

<b>5. ASSIMILATION OF MICROWAVE RADIANCE OBSERVATIONS FOR HURRICANE INITIALIZATION</b> .....	<b>52</b>
5.1 Assimilating Brightness Temperatures .....	52
5.2 Assimilating Synthetic SLP and Brightness Temperatures .....	57
<b>6. SUMMARY AND DISCUSSION</b> .....	<b>74</b>
<b>APPENDIX A: List of Acronyms</b> .....	<b>77</b>
<b>REFERENCES</b> .....	<b>79</b>
<b>BIOGRAPHICAL SKETCH</b> .....	<b>84</b>

## LIST OF TABLES

3.1	Values of $\Phi(\alpha)$ for $\theta$ in TLEXP1 and TLEXP2. . . . .	19
3.2	Values of $\Phi(\alpha)$ for $q_v$ in TLEXP1 and TLEXP2. . . . .	19
3.3	Values of $\Phi(\alpha)$ for $q_r$ and $q_r$ in TLEXP2. . . . .	20
3.4	Values for the Left and Right Hand Sides of Equation 3.2 for ADEXP1 and ADEXP2. . . . .	21
3.5	Value of $\phi(\alpha)$ for GREXP1 and GREXP1 . . . . .	22
3.6	Details of TWEXP1, TWEXP2, and TWEXP3. . . . .	23
4.1	Values for the intercept parameters used in the RTM based on the explicit moisture scheme used to compute the input. . . . .	35
4.2	Domain configurations for the hurricane forecasts whose data are used to calculate the background error covariance matrices and number of points from each domain used in the calculation. . . . .	48

## LIST OF FIGURES

2.1	Schematic of a poorly scaled problem (top) and a well scaled problem (bottom).	16
3.1	Initial SLP field (contoured every 4 hPa) produced by the COAMPS analysis scheme. The location of the the response function in Equation 3.4 is shown by the filled circle. . . . .	18
3.2	Normalized cost function values for TWEXP1, TWEXP2, and TWEXP3 for each iteration of the minimization procedure (15 total). The values were normalized by initial cost function value. . . . .	26
3.3	Normalized profiles of $J_{q_r}$ and $N_{q_r}$ for (a) TWEXP1 after the 5th iteration, (b) TWEXP2 after the the 1st iteration, and (c) TWEXP3 after the 1st iteration. Both $J_{q_r}$ and $N_{q_r}$ were normalized by their largest value. . . . .	27
3.4	The initial error (left) before the minimization procedure and final error (right) after the minimization procedure for $\theta$ at the model level $k = 20$ (approximately 1 km above the surface) for TWEXP3. The contour interval is 1 K. . . . .	28
3.5	Same as Figure 3.4 except for $q_r$ and the values have been multiplied by $1 \times 10^4$ . The contour interval is $1 \text{ kg kg}^{-1}$ . . . . .	28
3.6	The value of the cost function (top) and gradient norm (bottom) at each iteration of the minimization procedure in TWEXP4 and TWEXP5. . . . .	29
4.1	85V $T_{bs}$ produced by the RTM from a 24 h MM5 forecast using the GD scheme valid 0000 UTC 25 August 1998 (left), and observed 85V SSM/I $T_{bs}$ (right) from roughly the same time. $T_{bs}$ are in units of K. The filled circles indicates the observed center of Hurricane Bonnie at the forecast time. . . . .	36
4.2	Relative frequency of occurrence over three forecast domains of (a) 19V, (b) 22V, (c) 37V, and (d) 85V $T_{bs}$ . The $T_{bs}$ were placed in 5 K intervals, the observations are shown by the bins, while the $T_{bs}$ produced by the different explicit moisture schemes are shown as curves (the legend in graph differentiates between the schemes). The $T_{bs}$ were interpolated to grids with horizontal spacing of 56 km in (a) - (c) and 18 km in (d). . . . .	40
4.3	P1, P2, and P3 relative frequency plots of model-produced 85V $T_{bs}$ for the (a) GD, (b) R1, (c) R2, and (d) SH schemes. . . . .	41
4.4	Vertical background error correlation matrix of $q_c$ calculated using the data from (a) C1, (b) C2 (c) C3, and (d) C4. The standard deviations of the background error at each level in (a)-(d) are shown in (e). In (a)-(d), the contour interval is 0.2 and the axis labels correspond to height in kilometers. . .	46

4.5	Vertical background error correlation matrices of (a) $q_c$ , (b) $q_i$ , (c) $q_r$ , (d) $q_s$ , and (e) $q_g$ using data from 12 different hurricanes. The standard deviations of the background error at each level in (a)-(e) is shown in (f). In (a)-(d), the contour interval is 0.2 and the axis labels correspond to height in kilometers. . .	47
4.6	Normalized singular values (first five ordered from largest to smallest) for the vertical covariance matrices of $q_c$ , $q_i$ , $q_r$ , $q_s$ , and $q_g$ . . . . .	49
4.7	The full background error covariance matrix of $q_r$ (multiplied by $1 \times 10^7$ ) calculated using (a) all available singular values and (b) only the largest singular value. The contour interval is $1 \text{ kg}^2 \text{ kg}^{-2}$ . . . . .	50
4.8	Inverse the of vertical background error covariance matrix of (a) $q_c$ , (b) $q_i$ , (c) $q_r$ , (e) $q_s$ , and (e) $q_g$ . The values have been multiplied by $1.0 \times 10^{-5}$ and the axis labels correspond to height in kilometers. The contour intervals are (a) 0.25, (b) 0.75, (c) 0.02, (d) 0.05, and (e) $0.1 \text{ kg}^2 \text{ kg}^2$ . . . . .	51
5.1	Normalized value of the cost function for each channel (19V, 22V, 37V, and 85V) at each iteration of the minimization in ETB. The values were normalized by dividing by the respective initial value. . . . .	58
5.2	19V $T_b$ s from SSM/I observations (upper left), model-produced from the ETB analysis (upper right), and model-produced from the CNTRL analysis (bottom) at 12 UTC 23 August 1998 in units of K. The filled circles represents the observed center of Hurricane Bonnie, and the line in the upper left panel indicates the location of the cross section shown in Figures 5.8-5.9. . . . .	59
5.3	Initial analysis of $q_r$ (left) at $k = 15$ (approximately 5000 m) The contour interval is $0.1 \text{ g kg}^{-1}$ . and the filled circle indicates the observed center of Hurricane Bonnie. . . . .	60
5.4	Same as Figure 5.2 except for 22V $T_b$ s. . . . .	61
5.5	Same as Figure 5.4 except for 37V $T_b$ s. . . . .	62
5.6	Same as Figure 5.5 except for 85V $T_b$ s. . . . .	63
5.7	Same as figure 5.3 except for $q_s$ at model level $k = 12$ (approximately 8000 m). . . . .	64
5.8	Vertical cross section of $q_r$ analysis values for ETB (left) and ETBNBG (right) at $24.3^\circ \text{ N}$ . The contour interval is $0.1 \text{ g kg}^{-1}$ and the labels on the $z$ -axis refer to the height in m. The location of the cross section is indicated by the line in Figure 5.2. . . . .	64
5.9	Difference between 19V $T_b$ s from the SSM/I observations and the CNTRL analysis (CNTRL-SSM/I, black line), SSM/I observations and the ETB analysis, (ETB-SSM/I, blue dashed line), and SSM/I observations and the ETBNBG analysis (ETBNBG-SSM/I, red dot-dashed line) along the cross section at $24.3^\circ \text{ N}$ show in Figure 5.2. The $y$ -axis denotes the difference values in K. . . . .	65

5.10	Normalized profiles of the analysis values of $q_r$ for ETB (blue squares) and ETBNBG (red diamond) at 24.3°N and 69.0°W. The profiles were normalized by the largest value in the respective profile. The black dashed line is a profile of the correlation at 5 km in the $\mathbf{B}_{q_r}$ matrix shown in Figure 4.5. The labels on the $z$ -axis refer to the height in m. . . . .	66
5.11	Observed and forecasted minimum central SLP (left) and maximum surface wind speed (right) from ETB and CNTRL of Hurricane Bonnie for the 24 h period beginning 1200 UTC 23 August 1998. Units are in hPa (left) and $\text{m s}^{-1}$ . . . . .	66
5.12	Observed (black circles) and forecasted track from ETB (blue squares) and CNTRL (red triangles) of Hurricane Bonnie for the 24 h period beginning 1200 UTC 23 August 1998. . . . .	67
5.13	Averaged value of $q_r$ for ETB and CNTRL for the 24 h forecasts at model level $k = 15$ (approximately 5 km) in a 150 km $\times$ 150 km box on the eastern side of the storm. The box was positioned on the eastern side of the hurricane always at the same position relative to the storm's center. . . . .	68
5.14	19V $T_b$ s from SSM/I observations (upper left), model-produced from the 24 h ETB forecast (upper right) and the 24 h CNTRL forecast (lower) at 00 UTC 24 August 1998 in units of K. The filled circle represents the observed (upper left) or forecasted (upper right and bottom) center of Hurricane Bonnie. . . . .	69
5.15	Same as Figure 5.14 except for 85V $T_b$ s. . . . .	70
5.16	Observed and forecasted minimum central SLP (left) and maximum surface windspeed (right) from EBOTH and EBDA of Hurricane Bonnie for the 24 h period beginning 1200 UTC 23 August 1998. Units are in hPa (left) and $\text{m s}^{-1}$ . . . . .	71
5.17	Observed (black circles) and forecasted track from EBOTH (blue squares) and EBDA (red diamonds) of Hurricane Bonnie for the 24 h period beginning 1200 UTC 23 August 1998. . . . .	71
5.18	Model-produced 19V $T_b$ s from the initial analysis in EBDA (left) and EBOTH (right) at 12 UTC 23 August 1998 in units of K. The filled circle represents the analyzed center of Hurricane Bonnie. . . . .	72
5.19	Same as Figure 5.18 except for the 85V $T_b$ s. . . . .	72
5.20	Same as Figure 5.18 except for 24 h forecast. . . . .	73
5.21	Same as Figure 5.19 except for 24 h forecast. . . . .	73

## ABSTRACT

An adjoint mesoscale modeling system based on the Naval Research Laboratory's Coupled Ocean Atmosphere Mesoscale Prediction System (COAMPS) atmospheric model was created for use in sensitivity and data assimilation experiments. In addition to the tangent linear and adjoint models of the dynamical core of the COAMPS model, the system includes the tangent linear and adjoint models of the boundary layer turbulent kinetic energy, cumulus, and explicit moist physics parameterizations. The inclusion of these adjoint model physics schemes allows for assimilation experiments involving rain-affected observations such as microwave radiances.

A radiative transfer model which includes the effects of hydrometeors on atmospheric radiation was linked to the adjoint modeling system to assimilate microwave radiance observations. Probability distribution functions of model-produced and SSM/I observed brightness temperatures show that the mesoscale prediction overestimates the areas of precipitation, but overall matches the microwave observations quite well. Furthermore, estimates of vertical background error covariance matrices for the hydrometeor variables were calculated using differences between model forecasts which utilized different explicit moisture schemes. The statistics of the differences between the forecasts were assumed to be the same as the statistics of the background error for these variables. The inverse of these matrices (which are needed for data assimilation) were computed using Singular Value Decomposition. Only the largest singular value was kept in calculating the inverse. This ensured that all of the elements of the inverse matrix were non-negative.

Finally, microwave radiance observations for Hurricane Bonnie (1998) were assimilated in a 4-dimensional variational data assimilation framework using the COAMPS adjoint model. The model-produced radiances calculated from the analysis fields after the assimilation process match the observations well for the lower frequency channels which are sensitive to liquid precipitation and water vapor. In the highest frequency channel, where the presence of frozen hydrometeors can have a large impact on the radiance value, the match between the

analysis and the observations was not as good. The forecasted hurricane was slightly stronger after the assimilation of microwave radiances in terms of both maximum surface windspeed and minimum central sea level pressure, and some improvement was seen in radiance space as well. More observations from within the hurricane, which will improve the analysis of other variables, will most likely be needed to see a greater forecast impact from the assimilation of these observations.

# CHAPTER 1

## INTRODUCTION

Adjoint models are important tools in meteorology and oceanography because they allow for the efficient computation of the gradient of any scalar value derived from a model's forecast with respect to the model's input control variables. Adjoint models are often employed in variational data assimilation to calculate the gradient of a scalar cost function that measures the difference between a model's control variable and observations. The gradient is used by an iterative minimization scheme to reduce the value of the cost function by modifying the model's input variables. For problems in which the adjoint of a numerical weather prediction (NWP) model is available, observations can be assimilated over a range of times so that the model's solution will be closer in value to the observations at their observed times within the assimilation window, not just at the initial time, while satisfying the dynamical and physical constraints of the forecast model. These types of problems fall into the class of 4-dimensional variational (4D-Var) assimilation.

The use of adjoint models in atmospheric data assimilation was first proposed by LeDimet and Talagrand [1]. In the years following, a number of 4D-Var data assimilation systems have been developed which utilize simple [2] and primitive equation models [3] [4] [5] [6] [7] [8]. The majority of present day 4D-Var systems are based on global NWP models and have been applied to synoptic and larger scale situations.

On the mesoscale, 4D-Var assimilation techniques remain relatively untested in an operational environment when compared to larger scales [9]. A number of factors have contributed to the lack of operational applications of 4D-Var data assimilation. These include: i) the increased computational cost due to the smaller spatial scales and associated time step, ii) the increased nonlinearity and discontinuous nature of the problem due to complex parameterizations which are required for accurate representation of atmospheric processes on smaller scales, iii) the lack of error estimates for model variables and observations

on smaller scales, iv) the inadequate number of conventional observations on small scales, and v) the expense of creating adjoint observation operators which are required to assimilate indirect satellite observations. Still, a number of studies have been conducted which show the promise of applying the 4D-Var technique to the mesoscale [10] [11] [12] [13] [14] [15] [16] [17].

One area of data assimilation which remains a challenge on the mesoscale, as well as on larger scales, is the assimilation of rain-affected observations, in particular satellite microwave radiances. Direct assimilation of satellite radiances was first proposed by Eyre et al. [18], and a number of succeeding studies have shown the value of assimilating radiances in cloud-free areas [19] [8]. More recent studies have focused on the possibility of assimilating radiances in cloudy areas to improve analyses and forecasts of precipitation. For global models, microwave radiances have been assimilated in a two step process in areas of precipitation [20] [21]. In the first step, a one-dimensional variational (1D-Var) assimilation technique is applied to a background field (obtained from a prior forecast) and the radiance observations to produce increments to the background field. In the second step, the 1D-Var increments are applied to the background field and the resulting values are assimilated as an observational field in a 4D-Var process. On the mesoscale, Vukicevic [17] conducted 4D-Var experiments whereby the representation of analyzed cloud structures was improved by assimilating rain-affected visible and infrared radiances. These studies have shown that the assimilation process can improve the analysis of precipitation fields, but little work has been done to investigate the forecast impact of these improved analyses.

In this study, an adjoint mesoscale modeling system suitable for variational assimilation and sensitivity experiments is developed, which includes the tangent linear and adjoint models of the Naval Research Laboratory's (NRL) Coupled Ocean Atmosphere Mesoscale Prediction System (COAMPS<sup>TM</sup>)<sup>1</sup> atmospheric model. The adjoint model of the COAMPS explicit moisture scheme is included in the system, which allows for the assimilation of rain-affected observations. Hydrometeor values are included in the model's state vector, which means the model's initial representation of precipitation fields can be improved through assimilation experiments. However, the inclusion of the explicit moist physics parameterization and the hydrometeor variables introduces nonlinearities and discontinuities

---

<sup>1</sup>COAMPS<sup>TM</sup> is a trademark of the Naval Research Laboratory.

that can adversely affect the performance of the minimization procedure in assimilation experiments. A number of tests are conducted that show how the model can best be utilized to produce acceptable behaviors in the assimilation process.

A radiative transfer model (RTM) developed by Liu [22] that includes the effects of hydrometeors on atmospheric radiation was linked to the adjoint modeling system to assimilate microwave radiance observations. The RTM computes microwave radiances, or brightness temperatures  $T_b$ s, from the COAMPS model variables. The tangent linear and adjoint models of the RTM, which were developed by Amerault and Zou [23], were also linked to the system. The RTM was updated to better simulate observed microwave  $T_b$ s. Previously, large differences between observed and model-produced  $T_b$ s occurred at higher frequencies in areas of large ice concentrations produced by the NWP model, but these differences have now been significantly reduced. Similar to the work of Chevallier and Bauer [24], who examined probability distribution functions (PDFs) of model-produced and observed  $T_b$ s using global NWP model data, we show that the newly updated RTM using mesoscale model fields as input is able to produce  $T_b$ s with similar PDF distributions as the observations.

In addition to having adjoint models corresponding to the NWP model and its associated observation operators, estimates of error values for the observations and background field are required for the 4D-Var procedure. Statistical estimates of observation errors are usually supplied by the instrument manufacturer and assumed to be uncorrelated. A number of studies [25] [26] [27] [28] [29] have been conducted to estimate the background error of conventional model variables (i.e. wind, pressure, temperature), but relatively little work [20] has been done to specify background error values for non-conventional variables such as hydrometeor values. For this work, we have computed estimates of background error covariances for five classes of hydrometeors (cloud water, cloud ice, rain water, snow, and graupel) by assuming that the statistics of differences between forecasts using different explicit moisture schemes is similar to the statistics of the background error.

Finally, the COAMPS Adjoint Modeling System (COAMPS-AMS) and an incorporated RTM are used for a hurricane initialization case, whereby microwave radiance observations are used to improve the analyses of precipitation fields. We also investigate the impact the assimilation of these observations have on the hurricane's track and intensity forecasts.

The components of the COAMPS-AMS are discussed in Chapter 2, which include the forward atmospheric model, the tangent linear and adjoint models, the minimization scheme, and a preconditioner. Tests of the system are presented in Chapter 3 that show how the inclusion of the explicit moisture scheme can affect the minimization process. Chapter 4 contains PDFs of observed and model produced  $T_b$ s as well as estimates of the background error covariance for hydrometeor variables. In Chapter 5, results from the assimilation of microwave radiance observations in the analysis and forecast of a hurricane is presented. A summary and discussion of this work is given in Chapter 6.

## CHAPTER 2

### COAMPS ADJOINT MODELING SYSTEM

#### 2.1 COAMPS Nonlinear Model

In order to develop a correct COAMPS adjoint model, it is vital to have a general understanding of the forward model component. In addition to an atmospheric model, the COAMPS system contains an atmospheric analysis scheme and an ocean model that can be coupled to the atmospheric component. Also included in the system is an aerosol-tracer module. However, the tangent linear and adjoint models have only been developed for the atmospheric model. In this section we provide an overview of the COAMPS atmospheric model and the features which are important to the development of the adjoint model.

##### 2.1.1 Governing Equations

The COAMPS atmospheric model is based on the non-hydrostatic and compressible primitive equations of Klemp and Wilhelmson [30]. Included in the model are parameterizations for subgrid-scale mixing, surface fluxes, explicit moist physics, cumulus convective processes, and radiation. Predictive equations are included for the zonal wind  $u$ , meridional wind  $v$ , vertical velocity  $w$ , the dimensionless Exner pressure function  $\pi$ , the potential temperature  $\theta$ , water vapor  $q_v$ , and turbulent kinetic energy (TKE)  $e$ . The explicit moist physics scheme allows for future values of cloud droplets  $q_c$ , cloud ice  $q_i$ , rain water  $q_r$ , snow  $q_s$ , and graupel  $q_g$  to be predicted. The full list of equations is given in Hodur [31].

For real data simulations, the lateral boundary conditions can be determined by the method of either Perkey-Krietzberg [32] or Davies [33]. These are the only lateral boundary conditions supported in the tangent linear and adjoint models. Both methods use NOGAPS (Navy Operational Global Atmospheric Prediction System) fields and a blending method to

determine the values of the fields at the boundaries. The Perkey-Krietzberg method utilizes the NOGAPS tendency fields while the Davies method utilizes the actual NOGAPS fields to calculate the model fields near the boundaries. The blending region usually consists of seven points. The points directly on the boundary are determined entirely from the NOGAPS fields and points within seven grid points of the boundary are a linear combination of the NOGAPS and COAMPS values, with the NOGAPS fields having a greater influence closer to the boundary and the COAMPS fields having a greater influence closer to the interior of the domain.

The nonhydrostatic equations allow for the propagation of fast moving sound waves which severely limits the length of the time step. In integrating the model, the terms which are responsible for sound waves are separated from the other terms and are moved forward in time using a time step smaller than the one used for the slower terms. The semi-implicit vertical differencing and the quasi-compressible assumption limits the speed of sound to be much less than the speed of sound in typical atmospheric conditions and therefore allows for larger values of the faster time step than if these assumptions were not utilized. The slower terms are integrated using a centered second-order leapfrog time differencing scheme (except at the initial time when a first-order forward time step is utilized).

### 2.1.2 Parameterizations

Those terms which cannot be explicitly determined in the governing equations for a specified model resolution have been parameterized. The predictive equation for  $e$  is parameterized following Mellor and Yamada [34]. This parameterization allows for an eddy coefficient to vary with height and a turbulent length scale to depend on the static stability. At the surface, the vertical fluxes are determined by the method outlined by Louis [35]. The calculation of the subgrid-scale mixing is based on the method of Deardorff [36]. The radiative parameterization, which contributes to the sources and sinks of heat in prognostic equation for  $\theta$ , is based on the scheme developed by Harshvardhan [37]. Included in this scheme are contributions from absorption and reflection of shortwave radiation and absorption and emission of longwave radiation. Clouds, stratiform and cumulus, are considered blackbody radiators and their spatial and temporal coverage is determined from model forecasts.

The cumulus parameterization, which modifies the temperature, water vapor and cloud-water profiles, is based on the work of Kain and Fritsch [38]. This scheme allows for a two way exchange of mass between the cloud and environment at each level in the model. The less complex Kuo [39] cumulus parameterization scheme is also an option in the COAMPS system.

The source and sink terms of the explicit moisture scheme are based on the work of Rutledge and Hobbs [40] and include updates from more recent studies [41] [42]. The moisture scheme allows for interactions between all of the moisture variables (cloud water  $q_c$ , cloud ice  $q_i$ , rain water  $q_r$ , snow  $q_s$ , graupel  $q_g$ , and water vapor  $q_v$ ) which includes processes such as evaporation, condensation, freezing, and melting. The size distribution of precipitating liquid drops and ice crystals are assumed to follow an inverse exponential function [43]:

$$N_x(D_x) = N_{x0} \exp(-\lambda D_x), \quad (2.1)$$

where,

$$\lambda = \left( \frac{\pi \rho_x N_{x0}}{\rho_v q_x} \right)^{0.25}, \quad (2.2)$$

and  $N_x(D_x)$  is the number of drops with diameters between  $D_x$  and  $D_x + dD_x$  for hydrometeor class  $x$  ( $x = r$  for rain,  $x = s$  for snow, and  $x = g$  for graupel). The mixing ratio of a hydrometeor class is given by  $q_x$  and the density by  $\rho_x$ , while  $\rho_v$  is the density of the moist air.  $N_{x0}$  is known as the intercept parameter, and  $\lambda$  is referred to as the slope. This is a single moment scheme for the precipitating hydrometeors, meaning that  $N_{x0}$  is a constant. In dual moments schemes,  $N_x$  is a predictive variable and  $N_{x0}$  can be diagnosed at every time step. This is the case for cloud ice where  $N_i$  is a predictive variable of the model. Many of the source and sink terms in this moisture schemes are based on the parameters in (2.1) and (2.2).

Not all of the parameterizations mentioned above have corresponding adjoints in the COAMPS-AMS. In addition to the dynamical core of the model, the adjoints of the boundary layer TKE, explicit moist physics, and Kuo cumulus scheme are included in the COAMPS-AMS. The radiation and Kain-Fritsch cumulus schemes are not supported in the COAMPS-AMS.

### 2.1.3 Parallel Processing

The forward nonlinear COAMPS atmospheric model was written for use in distributed memory environments. In multi-processor settings, the horizontal domain is decomposed into smaller sub-domains and each processor works on a separate part of the horizontal domain with communication between processors achieved through calls to a library of MPI (Message Passing Interface) subroutines. The tangent linear and adjoint models of the COAMPS-AMS, as well as the minimization routines have also been developed to work in the same type of multi-processor computing environments using MPI communication. This significantly reduces the computational time required for experiments involving the COAMPS adjoint model.

### 2.1.4 Analysis Scheme

The COAMPS analysis scheme uses a multivariate optimum interpolation (MVOI) technique [44] to map observations to the model grid at the initial time. Even though the COAMPS-AMS can be used to assimilate observations and create analysis fields, the regular analysis scheme of the COAMPS system is needed because the COAMPS-AMS is not a fully operational 4D-Var system. In its present form, it is a research tool that can be used to study the impact that the assimilation of new observations can have on analyses and forecasts. The original COAMPS analysis scheme is used to supply a background field for 4D-Var experiments.

## 2.2 Tangent Linear and Adjoint Models

An adjoint model allows for a variety of experiments in which the gradient of a particular aspect of a model's output with respect to the model's input needs to be calculated. More information on the wide range of applications in which adjoint models are employed can be found in Zou et al. [6]. In order to formulate an adjoint model, the original forward model must be linear, or if the model is nonlinear, as is the case with the COAMPS atmospheric model, the forward model must be linearized around the nonlinear model's trajectory, known as the basic state. Given a nonlinear model operator  $H$ , the tangent linear model operator  $\mathbf{H}$  is given as

$$\mathbf{H} = \frac{\partial H}{\partial \mathbf{x}}, \quad (2.3)$$

where  $\mathbf{x}$  is the state vector of the model. The tangent linear model is formulated by linearizing each line of code which depends on the state variables of the model. In the case of the COAMPS atmospheric model, each line which is related to the prognostic variables  $u$ ,  $v$ ,  $w$ ,  $\theta$ ,  $\pi$ ,  $e$ ,  $q_v$ ,  $q_c$ ,  $q_r$ ,  $q_i$ ,  $q_s$ ,  $q_g$ , and  $N_i$ , or any quantities derived from these prognostic variables is linearized. A typical assignment statement in the model has the form (as a mathematical expression)

$$y = f(x_1, x_2, \dots, x_m), \quad (2.4)$$

where  $x_1, x_2, \dots, x_m$  are input variables,  $f$  is a differentiable function, and  $y$  is a single output variable. Using the chain rule of differentiation gives:

$$\delta y = \frac{\partial f}{\partial x_1} \delta x_1 + \frac{\partial f}{\partial x_2} \delta x_2 + \dots + \frac{\partial f}{\partial x_m} \delta x_m, \quad (2.5)$$

where  $\delta x_1, \delta x_2, \dots, \delta x_m$  are the tangent linear input and  $\delta y$  is the tangent linear output.

The adjoint model is developed by realizing the transpose of the tangent linear model. The term ‘‘adjoint’’ comes from the inner product in linear space. A linear operator  $L^*$  is said to be the adjoint of  $L$  if for all  $\mathbf{c}$  and  $\mathbf{d}$  in linear space

$$\langle \mathbf{c}, L\mathbf{d} \rangle = \langle L^*\mathbf{d}, \mathbf{c} \rangle. \quad (2.6)$$

In Euclidean real number space,  $L^* = L^T$ , so that for our tangent linear model  $\mathbf{H}$ , the adjoint is written as  $\mathbf{H}^T$ . The adjoint of Equation 2.5 can be written as

$$\begin{aligned} \delta \tilde{x}_m &= \frac{\partial f}{\partial x_m} \delta \tilde{y} \\ &\vdots \\ \delta \tilde{x}_2 &= \frac{\partial f}{\partial x_2} \delta \tilde{y} \\ \delta \tilde{x}_1 &= \frac{\partial f}{\partial x_1} \delta \tilde{y}, \end{aligned} \quad (2.7)$$

where  $\delta \tilde{y}$  is the adjoint input and  $\delta \tilde{x}_1, \delta \tilde{x}_2, \dots, \delta \tilde{x}_m$  are the adjoint output.

The adjoint model runs in reverse order of the tangent linear model, meaning that the first line of code in the adjoint model corresponds to the last line of code in the tangent linear

model. Also in the adjoint model, the variables that were input in the adjoint model are now output, and those that were output are now input. Another important consideration of the adjoint model, is that while the model is running backwards, the basic state coefficients must be the same as those that were calculated in the tangent linear model. This means that the basic state must be calculated in the forward direction while the adjoint model is running in reverse. This requirement can significantly increase the computational resources necessary for adjoint model runs in terms of either time or memory. More details on the actual steps that must be followed in coding tangent linear and adjoint models are given in Zou et al. [6].

### **2.2.1 Automatic Adjoint Generation**

The tangent linear and adjoint code for the cumulus parameterization and the moist physics were developed using the Tangent Linear and Adjoint Model Compiler (TAMC) [45]. The automatically generated tangent linear code was correct in almost all cases (methods of testing tangent linear and adjoint code are given in Chapter 3). For the adjoint code, TAMC often had difficulties recalculating the basic state coefficients for variables which were repeatedly updated in the forward model. Therefore, the adjoint code generated by TAMC had to be altered manually in order to obtain a correct adjoint model. Even with the insufficiencies of TAMC, the amount of time needed to develop these sections was still significantly less than had the code been entirely produced by hand.

### **2.2.2 Discontinuities**

Tangent linear and adjoint models were developed for physical parameterizations in the COAMPS-AMS (the boundary layer TKE scheme, the cumulus parameterization, and the explicit moist physics scheme) which contain discontinuous processes due to the presence of “on-off” switches usually controlled by FORTRAN `if-then` statements in the model. A diabatic model which includes these processes is desirable in the assimilation process because it more faithfully reproduces the actual state of the atmosphere than an adiabatic model. However, the tangent linear and adjoint model formulations are based on continuous and differentiable systems of equations [1]. According to Zou [46], linearizing the nonlinear

model around the basic state to get the tangent linear model, and transposing it to obtain the adjoint model at every time step, while keeping the “on-off” switches the same in the tangent linear and adjoint models as they are in the nonlinear model at each time step of the integration, leads to suitable models for 4D-Var type experiments. The gradient calculated by the adjoint model is used to find a descent direction to minimize a cost function (more details of the minimization process are provided in Chapter 2.3.2), so the adjoint model only needs to lead the minimization process in the general direction of the minimum. Tests have shown that adjoint NWP models which include discontinuous physical processes produce gradients that lead to a convergence of the minimization procedure and an improved analysis field [46] [47]. The tests for correctness of the tangent linear model and gradient produced by the adjoint model (Chapter 3) should also hold in the presence of discontinuities as long as the perturbations used in the test are “very small” (small enough so that higher than first order terms can be ignored and large enough to avoid machine round-off errors).

## 2.3 Variational Data Assimilation

### 2.3.1 4D-Var Formulation

Adjoint models play a vital role in variational atmospheric assimilation, where the value of a scalar cost function, which measures in a quadratic sense the misfit between model variables to both observations and a background field, is minimized. The following equation is a typical example of a cost function for a variational assimilation problem is

$$J(\mathbf{x}) = \frac{1}{2}(H(\mathbf{x}) - \mathbf{y}^{\text{obs}})^T(\mathbf{O} + \mathbf{F})^{-1}(H(\mathbf{x}) - \mathbf{y}^{\text{obs}}) + \frac{1}{2}(\mathbf{x} - \mathbf{x}^b)^T\mathbf{B}^{-1}(\mathbf{x} - \mathbf{x}^b), \quad (2.9)$$

where  $H$  can be a combination of a forecast model and observation operators which transform the atmospheric state vector  $\mathbf{x}$  to the space of the observations  $\mathbf{y}^{\text{obs}}$ . The estimated error covariances of the observations and of  $H$  are contained in  $\mathbf{O}$  and  $\mathbf{F}$ , respectively. Background values (usually taken from a previous forecast) of the atmospheric state are contained in the vector  $\mathbf{x}^b$  and the error covariances of the background field are contained in the matrix  $\mathbf{B}$ .

In order to find the best estimate of  $\mathbf{x}$  which minimizes the value of  $J(\mathbf{x})$ , an iterative minimization procedure is employed to find a sequence  $n$  of  $\mathbf{x}$ :  $\mathbf{x}_0, \mathbf{x}_1, \dots, \mathbf{x}_n$  where the value of  $J(\mathbf{x}_n)$  decreases as  $n$  increases. The gradient of  $J(\mathbf{x}_n)$  is needed at every iteration

to determine the search direction for most minimization algorithms (see Chapter 2.3.2). The following expression for the gradient of the cost function is obtained by differentiating Equation 2.9 with respect to  $\mathbf{x}$ :

$$\nabla J(\mathbf{x}) = \mathbf{H}^T(\mathbf{O} + \mathbf{F})^{-1}(H(\mathbf{x}) - \mathbf{y}^{\text{obs}}) + \mathbf{B}^{-1}(\mathbf{x} - \mathbf{x}^b). \quad (2.10)$$

In the expression for the gradient we see that the adjoint model  $\mathbf{H}^T$  arises. With the COAMPS atmospheric model and its adjoint, observations can be assimilated over a time window, making the COAMPS-AMS suitable for use in 4D-Var assimilation experiments.

### 2.3.2 Minimization

The minimization scheme of the COAMPS-AMS searches for smaller values of a scalar function (usually in a form similar to Equation 2.9) by adjusting the model's input variables. The minimization scheme requires two inputs: (i) the value of the function, and (ii) its gradient with respect to the model's input. The scalar function is calculated from forecasted model variables and the gradient of this function with respect to the input parameters of the model is computed by the adjoint model.

Newton's method is a minimization algorithm with a relatively fast convergence rate which uses both first and second derivative information of a function in order to minimize it. For multivariate problems of dimension  $N$  the first derivative information is stored in the gradient vector and the second derivative information is stored in the  $N \times N$  Hessian matrix. For problems of large dimension, such as those encountered in NWP applications where  $N$  is on the order of  $10^5 - 10^7$ , it is not feasible to calculate or store a full Hessian matrix. Therefore, limited memory Quasi-Newton methods have been developed which approximate the full Hessian matrix with information from a relatively small number of vectors of dimension  $N$ . Using an approximate Hessian somewhat sacrifices the convergence rate when compared to Newton's method, but it makes large dimension minimization problems possible.

The Quasi-Newton limited memory BFGS (Broyden, Fletcher, Goldfarb, and Shanno) method (LBFGS) [48] is the minimization algorithm of the COAMPS-AMS. The LBFGS scheme is a robust algorithm which has also been implemented with the MM5 (fifth generation Penn State / National Center for Atmospheric Research Mesoscale Model) Adjoint

Modeling System [6]. In the LBFGS method, new estimates of  $\mathbf{x}_{n+1}$  that minimize a function  $J(\mathbf{x})$  are found using the update formula

$$\mathbf{x}_{n+1} = \mathbf{x}_n + \alpha_n \mathbf{d}_n, \quad (2.11)$$

where  $\mathbf{x}_n$  is a vector of length  $N$  containing values of the estimate of  $\mathbf{x}$  from the current iteration of the minimization. The step length is  $\alpha_n$ , and  $\mathbf{d}_n$  is the search direction given by

$$\mathbf{d}_n = -\mathbf{G}_n^{-1} \nabla J(\mathbf{x}_n), \quad (2.12)$$

where  $\mathbf{G}_n$  is the approximation to the Hessian. The gradient  $\nabla J(\mathbf{x}_n)$  is provided by the adjoint model. The step length  $\alpha_n$  is chosen to satisfy the strong Wolfe [49] conditions, which are:

$$J(\mathbf{x}_n + \alpha_n \mathbf{d}_n) \leq J(\mathbf{x}_n) + c_1 \alpha_n \nabla J(\mathbf{x}_n)^T \mathbf{d}_n, \quad (2.13)$$

$$|\nabla J(\mathbf{x}_n + \alpha_n \mathbf{d}_n)^T \mathbf{d}_n| \leq c_2 |\nabla J(\mathbf{x}_n)^T \mathbf{d}_n|, \quad (2.14)$$

where  $c_1 = 10^{-4}$  and  $c_2 = 0.9$ . The first condition ensures that there is decrease in the function. The second condition is known as the curvature conditions and is a check on the reduction of the norm of the the gradient. If the norm of the gradient increases greatly at the new location then it is a sign that further decrease in the function can be expected by moving along the search direction. The initial value of  $\alpha_n$  is chosen to be 1. If both of the strong Wolfe conditions are satisfied then the step size search terminates. Otherwise, the function and gradient information at  $\alpha_n = 0$  and  $\alpha_n = 1$  are used to create a cubic function of  $\alpha$  on the domain  $[0, 1]$  and a value of  $\alpha$  which minimizes the cubic function is found. This new value is chosen as  $\alpha_n$  and checked against the Wolfe conditions. If they are satisfied, then the search terminates; otherwise, the process of forming a cubic function on an updated interval is repeated until a satisfactory value of  $\alpha_n$  is found.

In the LBFGS method the full Hessian matrix is neither stored nor calculated. Instead the product  $\mathbf{G}_n^{-1} \nabla J(\mathbf{x}_n)$  is determined using the LBFGS update formula which incorporates information from the past  $m$  iterates of  $\mathbf{x}_n$  and  $\nabla J(\mathbf{x}_n)$  ( $m = 5$  in the COAMPS-AMS). Therefore, only a few vectors of length  $N$  need to be stored, instead of the entire  $N \times N$  matrix.

The LBFGS method to determine  $\mathbf{G}_n^{-1} \nabla J(\mathbf{x}_n)$  contains 2 loops. The following is a summary of the calculations performed at each iteration of the minimization procedure to determine this product.

- Initially, set  $\mathbf{q} = \nabla J(\mathbf{x}_n)$ ,  $\mathbf{s}_n = \mathbf{x}_{n+1} - \mathbf{x}_n$ ,  $\mathbf{y}_n = \nabla J(\mathbf{x}_{n+1}) - \nabla J(\mathbf{x}_n)$ ,  $\rho_n = \frac{1}{\mathbf{y}_n^T \mathbf{s}_n}$ , and  $\mathbf{Q} = \frac{\mathbf{y}_n^T \mathbf{s}_n}{\mathbf{y}_n^T \mathbf{y}_n} \mathbf{I}$ , where  $\mathbf{I}$  is the identity matrix.
- The first loop goes from  $i = n-1$  to  $n-m$ , and at each step  $\lambda_i = \rho_i \mathbf{s}_i^T \mathbf{q}$  and  $\mathbf{q} = \mathbf{q} - \lambda_i \mathbf{y}_i$  are calculated.
- After the first loop, set  $\mathbf{r} = \mathbf{Q}\mathbf{q}$
- In the second loop,  $i = n-m$  to  $n-1$ , and at each step  $\beta = \rho_i \mathbf{y}_i^T \mathbf{r}$  and  $\mathbf{r} = \mathbf{r} + \mathbf{s}_i(\lambda_i - \beta)$  are calculated.
- In the final step set  $\mathbf{G}_n^{-1} \nabla J(\mathbf{x}_n) = \mathbf{r}$

This process is repeated at each step of the minimization process to determine a new search direction  $\mathbf{d}_n$ .

It is also important to note that the model variable  $e$  is not included in  $\mathbf{x}$ . Even though the tangent linear and adjoint models of the boundary layer TKE scheme have been developed and tested for correctness, problems are often encountered in minimization experiments in which  $e$  is included in  $\mathbf{x}$ . Therefore, the boundary layer TKE parameterization is still used, but the variable  $e$  is never modified by the minimization process. Further work is needed to correctly scale  $e$  and improve the minimization procedure when it is included in the control vector.

### 2.3.3 Preconditioning

The vector  $\mathbf{x}$  contains values ranging over many orders of magnitude for variables with differing units. Therefore,  $\mathbf{x}$  must be properly scaled in order to non-dimensionalize the variables and formulate a well posed problem.

Figure 2.1 is a simple schematic which geometrically shows the effects scaling can have on minimization problems. The top panel shows contours of a two-dimensional function which is highly elliptical. This problem has not been scaled well; changes in the function value occur more rapidly in the vertical direction than they do the horizontal. If the initial guess of the minimizer of the function is located off the axes of the ellipse, a search direction determined by the negative gradient (the simplest way of choosing a search direction) will

not point toward the true minimum of the function. The bottom panel shows contours of a function which has been properly scaled. In this case the contours are more circular and the gradient of the function points in the direction of the minimum.

Scaling can also be thought of as preconditioning of the Hessian matrix. The convergence rate of the minimization procedure depends on the condition number (the ratio of the largest eigenvalue to the smallest eigenvalue) of the Hessian matrix. A condition number close to unity is desirable for fast convergence rates. Therefore, the Hessian is often pre-multiplied by a preconditioning matrix  $\mathbf{P}$  to form a new matrix with a lower condition number than the original Hessian matrix.

Zupanski [50] [51] developed a preconditioning method suitable for atmospheric 4-D Var problems. The symmetric and positive definite matrix  $\mathbf{P}$  can be written as:

$$\mathbf{P} = \mathbf{E}\mathbf{E}^T, \quad (2.15)$$

where

$$\mathbf{E} = \mathbf{S}^{1/2}\mathbf{\Gamma}^{1/2}. \quad (2.16)$$

Here,  $\mathbf{S}$  is a “rough” scaling matrix (the elements which make up  $\mathbf{S}$  are described below) and  $\mathbf{\Gamma}$  is a diagonal matrix containing the scaling factors. A scaling factor  $\gamma$  is calculated for each model variable  $c$  and at every model level  $k$  so that

$$\mathbf{\Gamma} = \text{diag}(\gamma_k^c). \quad (2.17)$$

In an effort to maximize the decrease in the cost function, Zupanski [50] derived the scaling factors as,

$$\gamma_k^c = \gamma_0 \frac{[J_k^c]^{1/2}}{[(\mathbf{g}^T \mathbf{R}^{-1} \mathbf{g})_k]^{1/2}}, \quad (2.18)$$

where  $J_k^c$  is the value of the cost function for model variable  $c$  at model level  $k$ ,  $\mathbf{g} = \nabla J$  is the gradient vector calculated by the adjoint model,  $\mathbf{R}$  is a diagonal matrix based on the observation error covariances in Equation 2.9 ( $\mathbf{R} \approx \mathbf{F} + \mathbf{O}$ ), and  $\gamma_0$  is an empirical parameter. The scaling factors are calculated after the initial run of the forward model (to calculate the numerator of Equation 2.18) and the adjoint model (to calculate the denominator of Equation 2.18). The constant  $\gamma_0$  can be altered to obtain better performance of the minimization process, but in most cases a value on the order of 1.0 will suffice. The

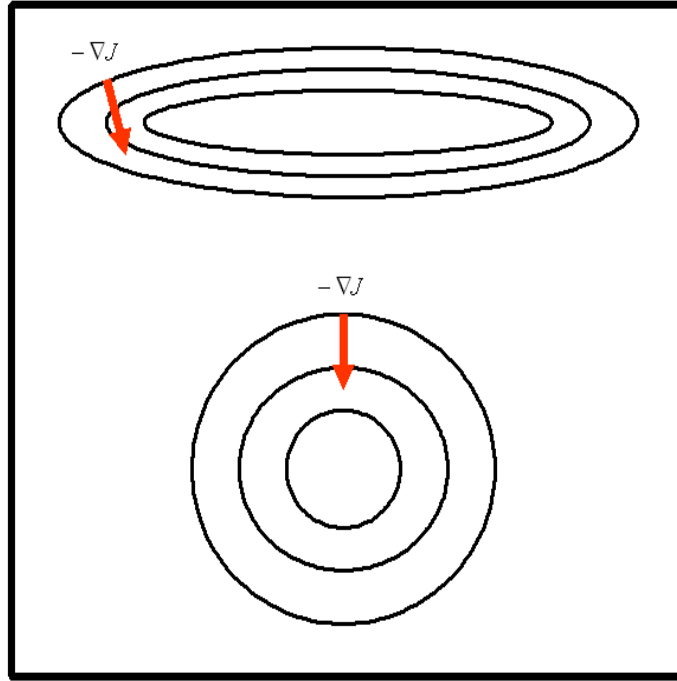


**Figure 2.1.** Schematic of a poorly scaled problem (top) and a well scaled problem (bottom).

scaling factors are calculated on model grid points, but the same method can be applied to situations where the observations do not lie on the model grid (which is much more realistic) with a few modifications [51].

In the COAMPS-AMS, the “rough” scaling ( $\mathbf{S}$ ) is a diagonal matrix that is calculated using forecast differences. For every 4D-Var experiment a short (6 h) forecast is run and the “rough” scaling factor  $s_k^c$  is taken to be the maximum absolute difference for variable  $c$  at level  $k$  between the analysis and the forecast. Therefore, the matrix  $\mathbf{S}$  is calculated first and set equal to  $\mathbf{P}$ . The matrix  $\mathbf{P}$  is then updated using Equations 2.15 and 2.16 if the appropriate options are selected to use the Zupanski scaling. In Chapter 3, we will look at the effect the Zupanski scaling parameters have on the minimization procedure.

## CHAPTER 3

### TESTS OF THE COAMPS ADJOINT MODEL

The tangent linear and adjoint models of the COAMPS-AMS have undergone a number of tests for correctness. In this chapter, we will present results from some of these tests to show that the system is correctly developed and suitable for use in sensitivity and assimilation experiments.

All the tests in this chapter were conducted using data from Hurricane Isabel (2003). Here, we will focus on forecasts beginning at 1200 UTC 14 September 2003. At this point, Isabel was a major hurricane (Category 4) with a minimum central sea level pressure (SLP) of 938 hPa and maximum surface windspeeds greater than  $65 \text{ m s}^{-1}$ . The model grid contained 30 vertical levels and  $49 \times 49$  points in the horizontal domain with 30 km spacing. The domain was centered in the Atlantic Ocean at  $-65.8^\circ \text{ W}$  and  $23.8^\circ \text{ N}$ . Figure 3.1 shows the extent of the domain as well as the large scale analysis of SLP at the initial time. The model's central SLP is much weaker than the observed central SLP (this issue will be addressed in Chapter 4.1). All test were performed on an SGI Origin 2000 using 8 processors.

#### 3.1 Testing the Tangent Linear Model

A correct tangent linear model will satisfy the following formula:

$$\Phi(\alpha) = \frac{\|H(\mathbf{x} + \alpha\mathbf{h}) - H(\mathbf{x})\|}{\|\alpha\mathbf{H}(\mathbf{x})\mathbf{h}\|} = 1 + O(\alpha), \quad (3.1)$$

where  $\mathbf{h}$  is the initial perturbation to  $\mathbf{x}$ . As  $\alpha$  gets smaller the value of  $\Phi(\alpha)$  approaches unity, up to the limit of the computer's accuracy, if the tangent linear model has been correctly formulated.

Tables 3.1 and 3.2 show the values of  $\Phi(\alpha)$  for 3 h model forecasts of  $\theta$  and  $q_v$ , respectively, at every point on the model grid, for two different tests of the tangent linear model. In the first experiment (TLEXP1), the cumulus and explicit moisture parameterizations were not

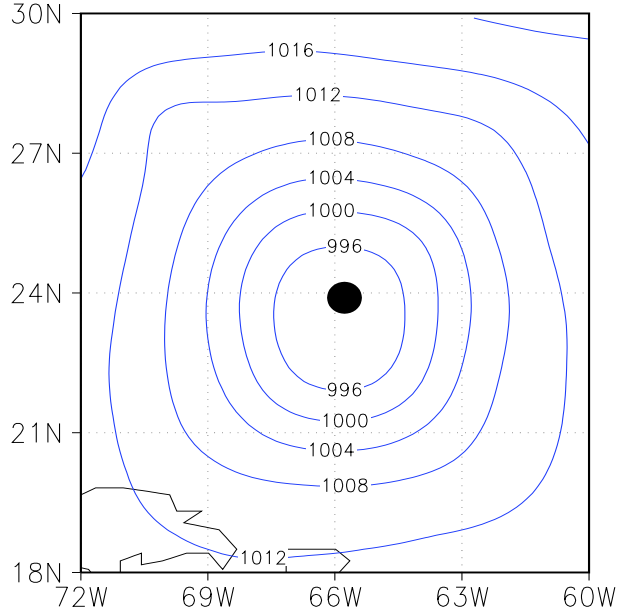


**Figure 3.1.** Initial SLP field (contoured every 4 hPa) produced by the COAMPS analysis scheme. The location of the the response function in Equation 3.4 is shown by the filled circle.

utilized, in the second experiment (TLEXP2), both schemes were used. In both experiments, a 6 h forecast valid at 1800 UTC September 14 2003 was used as input for the models. The difference between this forecast field and the initial analysis was used as the initial perturbation field  $\mathbf{h}$ . The nonlinear and tangent linear models were integrated forward in time for 3 h to obtain  $H(\mathbf{x})$  and  $\mathbf{H}(\mathbf{x})$ , respectively. The state vector  $\mathbf{x}$  was then perturbed a number of times, where each time the value of  $\alpha$  was decreased by an order of magnitude, to obtain  $H(\mathbf{x} + \alpha\mathbf{h})$  and calculate  $\Phi(\alpha)$ .

In TLEXP1, the value of  $\Phi(\alpha)$  is closest to unity when  $\alpha = 1 \times 10^{-6}$  for both  $\theta$  and  $q_v$ . For smaller values of  $\alpha$ , the value of  $\Phi(\alpha)$  moves away from unity because the limit of the computer's accuracy has been reached. When the moisture effects are included in TLEXP2,  $\Phi(\alpha)$  does not get closest to unity until  $\alpha$  is an order of magnitude smaller than in TLEXP1 ( $\alpha = 1 \times 10^{-7}$ ). The values of  $\Phi(\alpha)$  for  $q_s$  and  $q_r$  in TLEXP2 are shown in Table 3.3. As with  $\theta$  and  $q_v$  in TLEXP2, the value of  $\Phi(\alpha)$  for these hydrometeors is closest to unity when

**Table 3.1.** Values of  $\Phi(\alpha)$  for  $\theta$  in TLEXP1 and TLEXP2.

$\alpha$	$\Phi(\alpha)$	
	TLEXP1	TLEXP2
0.100E-04	0.9924753969	1.0574913686
0.100E-05	0.9496961068	1.0235025030
0.100E-06	1.0000001460	1.0000945573
0.100E-07	0.9999997800	0.9999990459
0.100E-08	1.0000224974	1.0000076976
0.100E-09	0.9999334105	1.0002972494
0.100E-10	1.0036603239	0.9964308845
0.100E-11	0.9807054602	1.0005004923
0.100E-12	1.0112680345	0.9026954339

**Table 3.2.** Values of  $\Phi(\alpha)$  for  $q_v$  in TLEXP1 and TLEXP2.

$\alpha$	$\Phi(\alpha)$	
	TLEXP1	TLEXP2
0.100E-04	1.0104348277	0.9785607286
0.100E-05	1.0390301018	0.9802922073
0.100E-06	1.0000000810	0.9997321606
0.100E-07	1.0000008105	1.0000040703
0.100E-08	0.9999973672	1.0000181817
0.100E-09	1.0000466451	1.0001212127
0.100E-10	0.9998478190	1.0029329413
0.100E-11	0.9999202232	1.0039926547
0.100E-12	0.9943518487	1.1480491391

$\alpha = 1 \times 10^{-7}$ . Even with the discontinuities in the moisture schemes, the tangent linear model is still correct for small enough values of  $\alpha$ .

### 3.2 Testing the Adjoint Model

For a correct adjoint model, the following equality will hold:

$$(\mathbf{H}(\mathbf{x})\mathbf{h})^T(\mathbf{H}(\mathbf{x})\mathbf{h}) = \mathbf{h}^T(\mathbf{H}^T(\mathbf{x})(\mathbf{H}(\mathbf{x})\mathbf{h})). \quad (3.2)$$

**Table 3.3.** Values of  $\Phi(\alpha)$  for  $q_r$  and  $q_s$  in TLEXP2.

$\alpha$	$\Phi(\alpha)$	
	$q_r$	$q_s$
0.100E-05	1.0380817549	1.2618354888
0.100E-06	0.9996305714	1.0003934488
0.100E-07	0.9999646467	1.0000087627
0.100E-08	0.9999473296	1.0000432662
0.100E-09	0.9998801962	1.0004572421
0.100E-10	0.9975892510	1.0050076663
0.100E-11	0.9777098828	0.9530330619
0.100E-12	1.0743762558	0.6792555126

Equation 3.2 simply states that the output of the tangent linear model dotted with itself (the left hand side of Equation 3.2) is equal to the dot product of the input to the tangent linear model and the result of the adjoint model integration using the output of the tangent linear model as input, (the right hand side of Equation 3.2). The two sides of the equation should match to the limit of the computer’s accuracy if the adjoint model has been correctly formulated from the corresponding tangent linear model.

The test of the adjoint model was conducted in a similar fashion to the tests of the tangent linear model. In the first test, ADEXP1, the cumulus and explicit moisture schemes were not included, while they were included in the second experiment, ADEXP2. The initial perturbation  $\mathbf{h}$  and state vector  $\mathbf{x}$  were the same as in TLEXP1 and TLEXP2. The tangent linear model was integrated forward in time for 3 h and the left hand side of Equation 3.2 was calculated. The output of the tangent linear model integration was used as input for the adjoint model, and it was integrated backward in time for 3 h to calculate the right hand side of Equation 3.2.

Table 3.4 shows the adjoint model tests results for ADEXP1 and ADEXP2. When no moisture effects were included, 15 digit accuracy was obtained. However, only 11 digit accuracy with the moisture parameterizations included. In other tests of the adjoint model that have been conducted, we have found that the two sides of Equation 3.2 match to at least 13 digits when the moisture parameterizations aren’t included and 11 digits when they are included.

**Table 3.4.** Values for the Left and Right Hand Sides of Equation 3.2 for ADEXP1 and ADEXP2.

	ADEXP1	ADEXP2
Left	0.1894326127049555E+07	0.1397878657343188E+15
Right	0.1894326127049560E+07	0.1397878657343712E+15

### 3.3 Gradient Check

With a correct tangent linear and adjoint model, a gradient check can be performed to ensure that an adjoint sensitivity or 4D-Var experiment has been properly coded. The gradient check is a way to test that  $J$  is being correctly calculated and the forcing terms  $\partial J/\partial \mathbf{x}(t)$  are properly inserted into the adjoint model. If all of these things have been done correctly then the following equation will hold:

$$\phi(\alpha) = \frac{J(\mathbf{x} + \alpha \nabla J(\mathbf{x})) - J(\mathbf{x})}{\alpha \nabla J(\mathbf{x})^T \nabla J(\mathbf{x})} = 1 + O(\alpha). \quad (3.3)$$

The behavior of  $\phi(\alpha)$  for a correct gradient is the same as  $\Phi(\alpha)$  in Equation 3.1 for a correct tangent linear model.

Here, we will perform a gradient check for a simple function  $J$  which is defined as

$$J = \pi_{25,25,30}^{6hr}, \quad (3.4)$$

or in words, the response function is equal to the value of the 6 h forecasted Exner pressure at the point  $i = 25$ ,  $j = 25$  on the model level closest to the surface ( $k = 30$ ). The response function's location was set near the center of Hurricane Isabel (the dot in Figure 3.1 represents the location of the response function). Again, two tests were conducted. In the first experiment, GREXP1 the cumulus and explicit moisture schemes were turned off during the model run, and in the second test, GREXP2, the schemes were turned back on.

The results of a gradient check for GREXP1 and GREXP2 are shown in Table 3.5. As in the tangent linear test (Chapter 3.1), the value of  $\phi(\alpha)$  approaches unity relatively smoothly when the moisture schemes are turned off. However, when the schemes are turned on,  $\alpha$  must become sufficiently small ( $\alpha = 1 \times 10^{-5}$ ) in order for  $\phi(\alpha)$  to approach unity.

**Table 3.5.** Value of  $\phi(\alpha)$  for GREXP1 and GREXP2

$\alpha$	$\phi(\alpha)$	
	GREXP1	GREXP2
0.100E-04	1.000000021	0.809226791
0.100E-05	1.000000030	1.006566795
0.100E-06	0.999999486	1.003397480
0.100E-07	0.999993335	1.000317690
0.100E-08	0.999981031	1.000037758
0.100E-09	0.999437636	1.000141231
0.100E-10	1.007844888	1.000650043
0.100E-11	1.004769064	1.008645666
0.100E-12	0.922747099	1.047554846

### 3.4 Twin Experiment

A final test of all of the 4D-Var assimilation components of the COAMPS-AMS is a twin experiment. In this type of experiment, a model forecast field is treated as the observational field, which means that the model and observations are defined on the same space. The problem is well posed because an observation exists for every model variable at every point so only an observational term is included in the cost function. Furthermore, the observations are consistent with the dynamical and physical constraints of the model.

For the experiments in this section, forecasts fields which are valid a short time (3 h) after the assimilation time will be used as the observations. For example, if the cost function was being calculated at the 1 h forecast time, then the 4 h forecast fields would be considered the “observations.” In other words, the minimization procedure is adjusting the model fields to forecast values which occur 3 h after the assimilation time. The cost function for these experiment is defined as

$$J(\mathbf{x}) = \frac{1}{2} \sum_{r=0,15,30,45,60\text{min}} (\mathbf{x}(t_r) - \mathbf{x}^{\text{obs}})^T \mathbf{W} (\mathbf{x}(t_r) - \mathbf{x}^{\text{obs}}), \quad (3.5)$$

where  $\mathbf{x}^{\text{obs}}$  are the “observations” generated by the forecast model and  $\mathbf{x}(t_r)$  is the model state vector at time  $t_r$ . The diagonal matrix  $\mathbf{W}$  contains the weightings terms  $\omega$  calculated for each variable  $c$  and at every level  $k$  using the formula,

**Table 3.6.** Details of TWEXP1, TWEXP2, and TWEXP3.

	TWEXP1	TWEXP2	TWEXP3
Initial guess of $\mathbf{x}$	Analysis Field	6 h forecast	6 h forecast
Zupanski Preconditioning	Yes	No	Yes
Forecast times used for $\mathbf{x}^{\text{obs}}$ (min)	180, 195, 210 225, and 240	540, 555, 570 585, and 600	540, 555, 570 585, and 600

$$\omega_k^c = \frac{1}{s_L^c}{}^2, \quad (3.6)$$

where  $s_k^c$  are the “rough” scaling factors defined in Chapter 2.3.3.

When the model state vector  $\mathbf{x}$  includes the hydrometeor and number concentration variables, choosing a proper initial guess of  $\mathbf{x}$  and preconditioning procedure is vital to the success of the minimization procedure. To illustrate this point, three different twin experiments were performed. Table 3.6 highlights the differences between the experiments. In the first twin experiment, TWEXP1, the initial guess of  $\mathbf{x}(t_0)$  is the COAMPS analysis field, which means that the observations are the 180, 195, 210, and 240 min forecast fields. Also for this experiment, the Zupanski preconditioning method (Chapter 2.3.3) is used to update the “rough” scaling factors. In TWEXP2, the initial guess of  $\mathbf{x}(t_0)$  is the 6 h forecast field; therefore, the observations are obtained from forecast fields which are valid exactly 6 h after forecast fields used for the observations in TWEXP1 (540, 555, 570, 585, and 600 min). In TWEXP2, the Zupanski preconditioning method is not applied to the “rough” scaling factors. Finally, the third experiment (TWEXP3) is the same as TWEXP2, except that the Zupanski preconditioning method has been applied to update the scaling parameters.

Figure 3.2 shows the value of the cost function (Equation 3.5) at each iteration of the minimization for TWEXP1, TWEXP2, and TWEXP3. In TWEXP1, some reduction in the cost function does occur (approximately 40%), but the minimization procedure fails to find a suitable step length after the fifth iteration. In TWEXP2, the minimization fails after the third iteration with virtually no decrease in the cost function. In TWEXP3, a substantial decrease in the cost function (almost 80%) occurs and the minimization shows signs of convergence by the end of the minimization (15 iterations). From these results, it is clear that the Zupanski preconditioning is extremely important to a minimization procedure

which includes hydrometeor variables in the state vector. Also, of importance is the initial estimate of  $\mathbf{x}(t_0)$ . The difference between TWEXP1 and TWEXP3 is in the choice of  $\mathbf{x}(t_0)$ . Starting from the COAMPS analysis field, in which the precipitation fields are zero, the minimization does not converge as well as in the case when the minimization begins from a forecast field, where the precipitation fields have been allowed to “spin-up.”

Figure 3.3 further illustrates these points. Here we show at each model level the value of the cost function due to  $q_r$

$$J_{q_r} = \frac{1}{2} \sum_{r=0,15,30,45,60\text{min}} (\mathbf{q}_r(t_r) - \mathbf{q}_r^{\text{obs}})^T \mathbf{W}_{q_r} (\mathbf{q}_r(t_r) - \mathbf{q}_r^{\text{obs}}), \quad (3.7)$$

and the norm of the gradient due to  $q_r$ ,

$$N_{q_r} = \left( \frac{\partial J}{\partial \mathbf{q}_r} \right)^T \left( \frac{\partial J}{\partial \mathbf{q}_r} \right). \quad (3.8)$$

The vectors  $\mathbf{q}_r$  and  $\mathbf{q}_r^{\text{obs}}$  are the portions of  $\mathbf{x}$  and  $\mathbf{x}^{\text{obs}}$ , respectively, corresponding to  $q_r$ , while the matrix  $\mathbf{W}_{q_r}$  is the portion of  $\mathbf{W}$  corresponding to  $q_r$ .

If the minimization is to work effectively, the norm of the gradient should be large in locations where the cost function is large and small in locations where the cost function is small. The norm of the gradient is a scalar measure of the magnitude of the gradient vector which is used to determine the descent direction. In areas where the contribution to the norm of the gradient is large, the largest changes in the cost function will occur when the minimization procedure modifies the control vector. Therefore, if the relative value of the cost function and the norm of the gradient agree at every location, the minimization procedure will be able to reduce the cost function in areas where it is largest while keeping it small in areas where it was initially small.

In Figure 3.3a,  $J_{q_r}$  and  $N_{q_r}$  at each model level are shown for TWEXP1 after the fifth iteration of the minimization process (a suitable step length could not be found after this iteration). The norm of the gradient is largest at level  $k = 16$ , while the cost function is largest at  $k = 14$ . In the lower levels ( $k = 17 - 30$ ) the cost function is relatively large, while the norm of the gradient is small. Figure 3.3b, is the same as Figure 3.3a, except that it is for TWEXP2 after the first iteration (almost no reduction in the cost function was observed for this experiment). Here, we see that the cost function is again largest at  $k = 14$  while the norm of the gradient is largest at  $k = 19$ . Furthermore, in the upper levels of the

model ( $k > 15$ ), the cost function is zero, while the norm of the gradient is still relatively large. Finally for TWEXP3, where the minimization procedure performed best, we see in Figure 3.3c that the shape of the cost function and gradient norm profiles after the first iteration (they remained in agreement at each iteration of the minimization process). This means that in the areas where the cost function is large, the minimization scheme will be able to effectively reduce those values using information provided by the gradient with a small step size, which will not increase the value of the cost function in areas where it is already small.

Figures 3.4 and 3.5 show the errors in the  $\theta$  and  $q_r$  fields, respectively, at the initial time before and after the minimization process for TWEXP3. For  $\theta$ , the magnitude of the initial error at 1 km is as large as 4 K. After the minimization, it is less than 1 K. The same type of reduction also occurs in the  $q_r$  field, where the error before the minimization is as large as  $4 \times 10^{-4} \text{ kg kg}^{-1}$ , and is less than  $1 \times 10^{-4} \text{ kg kg}^{-1}$  after the minimization process.

In TWEXP4 and TWEXP5, the hydrometeor and number concentration variables are excluded from the state vector to see the effect of the Zupanski preconditioning on the remaining variables. In these experiments, the success of the minimization process is less sensitive to the preconditioning method. In TWEXP4 the Zupanski preconditioning method is applied, while in TWEXP5, only the “rough” scaling values are used. For both experiments,  $\mathbf{x}(t_0)$  is the 6 h forecast field, but the hydrometeors values are not included in the vector. The explicit moisture scheme is turned on, but the hydrometeor values are treated as constants in the minimization experiment. Figure 3.6 shows the value of the total cost function and norm of the gradient for TWEXP4 and TWEXP5. When the Zupanski preconditioning is applied, the reduction in the cost function occurs more rapidly (almost 80%) reduction after 5 iterations, than in the case when it is not applied (only 20% reduction in first 5 iterations). This shows that the Zupanski preconditioning is performing as it was designed to do. However, the behavior of the norm of the gradient is similar between the two experiments (both have a total reduction of approximately 75%).

In this chapter we have demonstrated that the tangent linear and adjoint models of the COAMPS-AMS are working correctly. Some simple experiments have also demonstrated that the system is suitable for 4D-Var experiments. In Chapter 5, the COAMPS-AMS will be used to assimilate real observations.

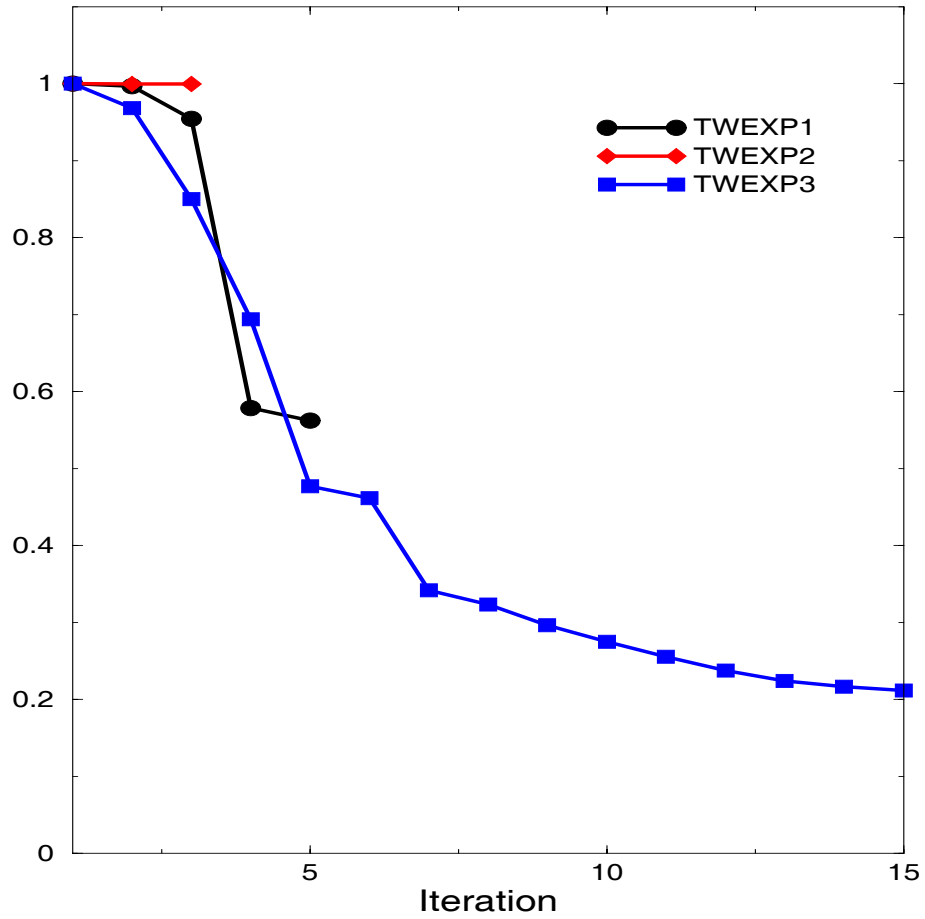


**Figure 3.2.** Normalized cost function values for TWEXP1, TWEXP2, and TWEXP3 for each iteration of the minimization procedure (15 total). The values were normalized by initial cost function value.

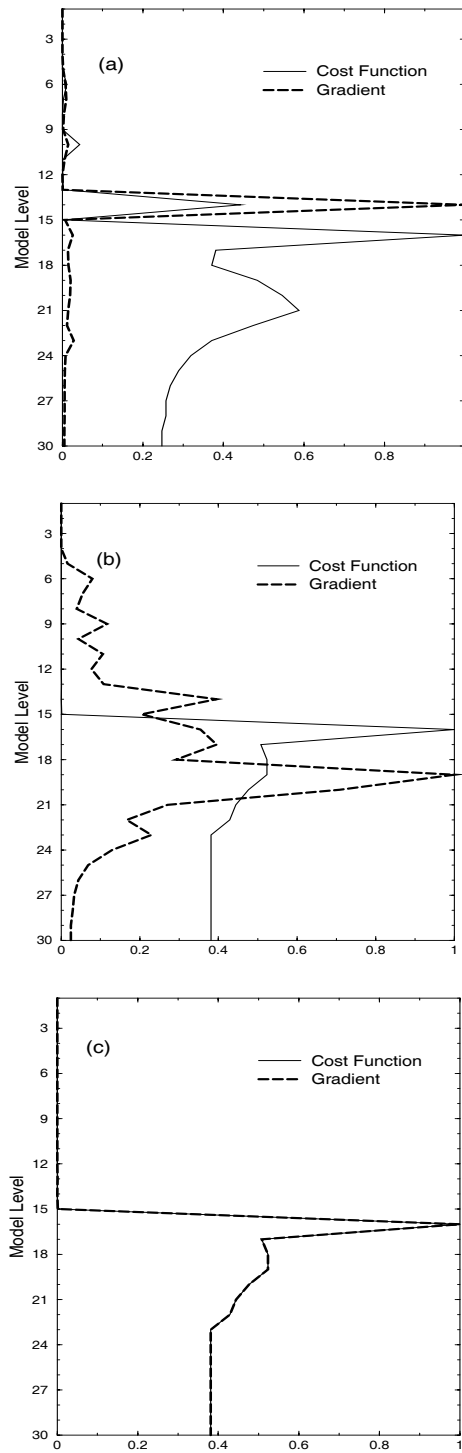


**Figure 3.3.** Normalized profiles of  $J_{q_r}$  and  $N_{q_r}$  for (a) TWEXP1 after the 5th iteration, (b) TWEXP2 after the the 1st iteration, and (c) TWEXP3 after the 1st iteration. Both  $J_{q_r}$  and  $N_{q_r}$  were normalized by their largest value.

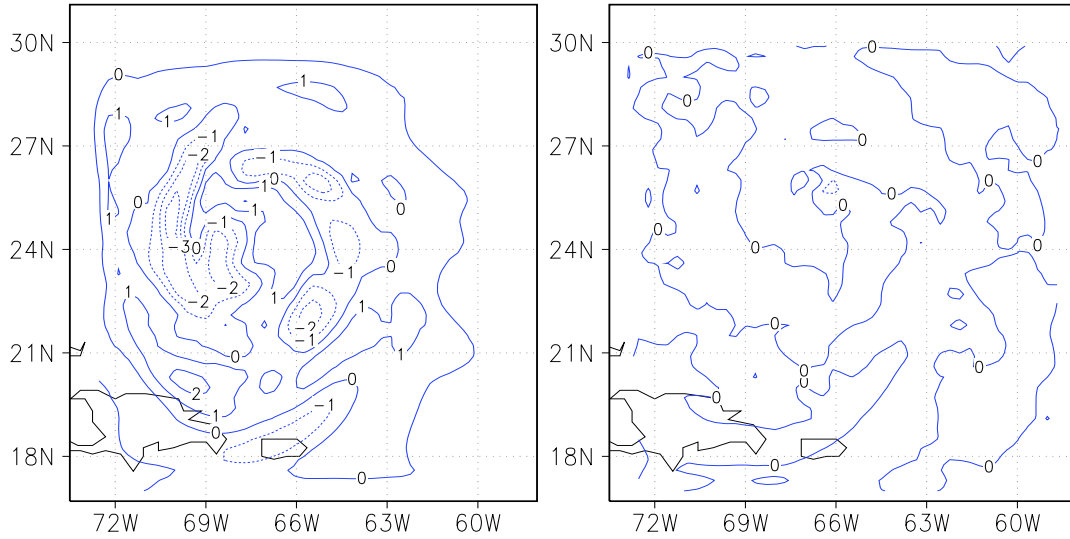


**Figure 3.4.** The initial error (left) before the minimization procedure and final error (right) after the minimization procedure for  $\theta$  at the model level  $k = 20$  (approximately 1 km above the surface) for TWEXP3. The contour interval is 1 K.

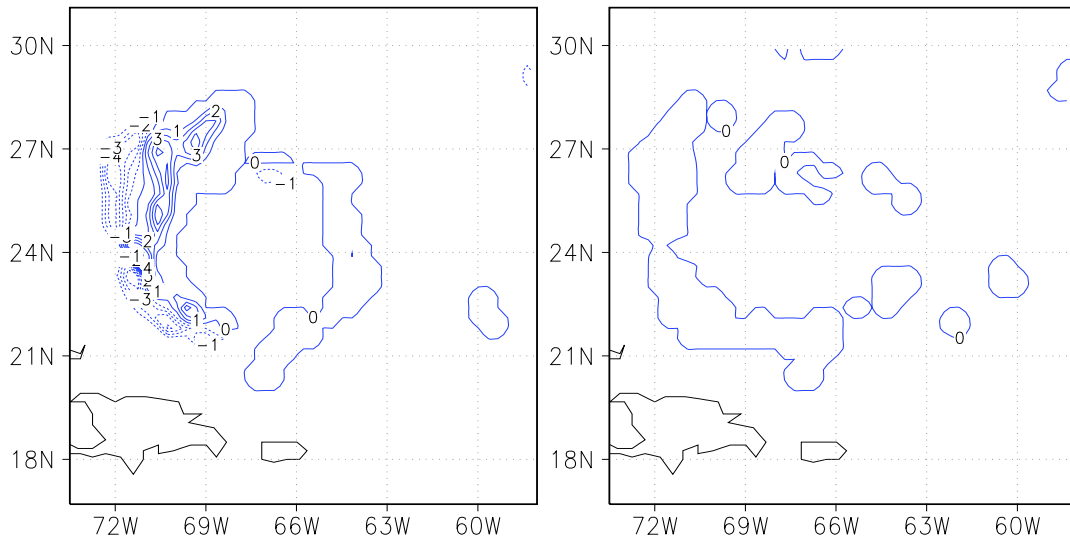


**Figure 3.5.** Same as Figure 3.4 except for  $q_r$  and the values have been multiplied by  $1 \times 10^4$ . The contour interval is  $1 \text{ kg kg}^{-1}$ .

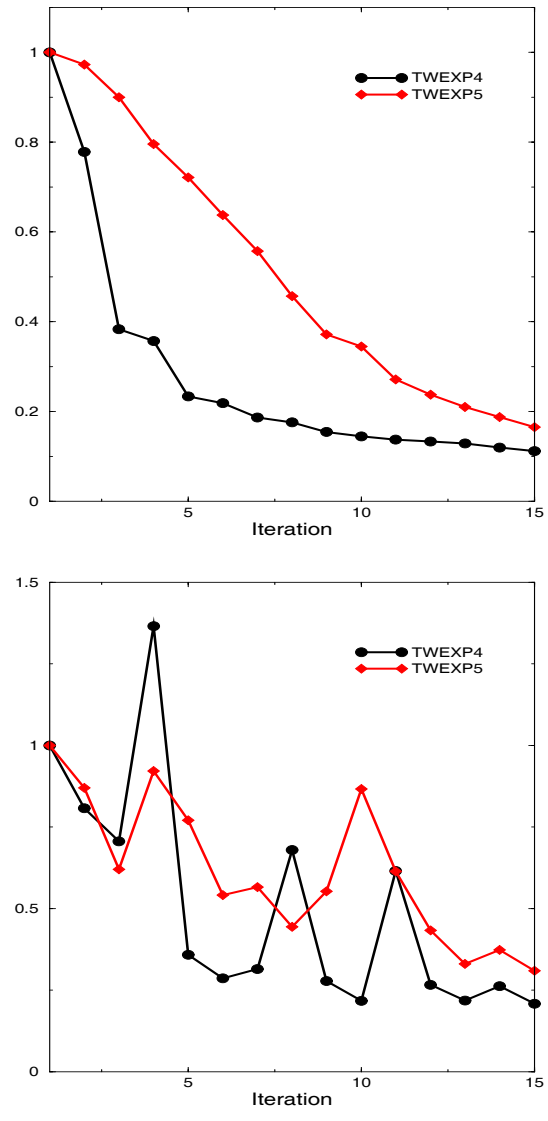


**Figure 3.6.** The value of the cost function (top) and gradient norm (bottom) at each iteration of the minimization procedure in TWEXP4 and TWEXP5.

## CHAPTER 4

# RTM PERFORMANCE AND BACKGROUND ERROR COVARIANCE ESTIMATES OF HYDROMETEOR VARIABLES

The eventual goal of this work is to assimilate  $T_b$ s in precipitating areas using the COAMPS-AMS. Before this can be done, we must ensure that the RTM can compute realistic  $T_b$ s from mesoscale NWP data. Here, we will use the MM5 model instead of the COAMPS atmospheric model because a number of options exist for the explicit moisture scheme in the MM5. This will allow us to explore some of the variability in the RTM calculations using different input data. Furthermore, the statistics of the differences between forecasts using different explicit moisture schemes will be used to estimate the background error covariance matrices of the hydrometeor variables.

### 4.1 MM5

The MM5 is a limited area non-hydrostatic mesoscale model, which utilizes a finite-differencing scheme [52]. It is typically utilized with horizontal grid spacings on the order of 1-100 km. A number of different physical parameterization options are available with the MM5. The explicit moisture schemes, which forecast the hydrometeor fields, are of most importance to this study.

In the MM5, there are eight different explicit moisture scheme options. Of these, only four include prediction of precipitating ice phase hydrometeors; two Reisner schemes (R1 and R2, [53]), the Goddard (GD) scheme [54], and the Schultz (SH) scheme [55]. Each of the schemes were designed to model cloud processes on small scales (1-10 km). The R2 and GD schemes were developed from cloud resolving models while the R1 and SH schemes were designed to be computationally efficient while retaining much of the information in

the more complex schemes. Each of the four schemes contains predictive equations for the mixing ratios of cloud water  $q_c$ , cloud ice  $q_i$ , rain water  $q_r$ , and snowflakes  $q_s$ . The R2, GD, and SH schemes also predict the mixing ratio of graupel  $q_g$ , and the R2 scheme includes additional prognostic equations for the total number concentrations of cloud ice  $N_i$ , snow  $N_s$ , and graupel  $N_g$ . All of the source/sink terms parameterized in the SH can be expressed in terms of the mixing ratio or specific density of the hydrometeors. The R1, R2, and GD schemes are based on the works of Lin et al. [56] and Rutledge and Hobbs [40], where the size distribution of precipitating liquid drops and ice crystals are assumed to follow an inverse exponential function. As with the explicit moisture scheme of the COAMPS atmospheric model, many of the source and sink terms in the R1, R2, and GD schemes are based on the parameters in Equations 2.1 and 2.2.

## 4.2 Microwave Radiance Observations

Microwave radiance data from the Special Sensor Microwave/Imager (SSM/I) were used as observational data in this chapter. The SSM/I is a seven channel passive radiometer which is part of the payload on polar orbiting Defense Meteorological Satellite Program (DMSP) satellites [57]. Both vertical and horizontal polarizations are observed at 19.35, 37.00, and 85.50 GHz, (channels 19V, 19H, 37V, 37H, 85V, and 85H), while only vertically polarized measurements are recorded at 22.235 GHz (channel 22V). The horizontal resolution of the 85 GHz observations is roughly 15 km, while the observations at all other frequencies have a coarser resolution of 60 km. SSM/I observations from three DMSP satellites (F11, F13, F14) were made available for this study. Two swathes over the tropical Atlantic Ocean from each satellite were provided daily (one at approximately 0000 UTC and the other at approximately 1200 UTC) from 21-29 August 1998. During this time Hurricane Bonnie (1998) was active over the region of interest. Bonnie reached hurricane strength on 22 August 1998 at 0600 UTC over the tropical Atlantic Ocean, and reached her maximum strength on 23 August at 1200 UTC as a category 3 hurricane with a minimum central SLP of 954 hPa and maximum surface winds over  $50 \text{ m s}^{-1}$ . She weakened slightly before making landfall in Wilmington, North Carolina on 27 August.

### 4.3 BDA

Given that  $T_b$ s are being calculated to compare with observations from a hurricane, the MM5 is initialized using the BDA scheme. As was seen in Figure 3.1, the initial vortex for mature tropical cyclones produced by the COAMPS MVOI (Chapter 2.1.4) analysis scheme is much too weak. The same is also true of the MM5 analysis scheme. The BDA scheme remedies this problem.

The BDA scheme assimilates a synthetic SLP field, which is generated from a few observed parameters, in a 4D-Var data assimilation framework. This scheme is an attractive hurricane initialization method because the synthetic observations can be easily calculated and the short assimilation window makes the computational expense relatively cheap.

The synthetic SLP fields are created using Fujita's formula [58]. The SLP at a particular model grid point is specified as a function of the radial distance  $r_d$  from the grid point to the hurricane center,

$$P_{bogus}(r_d) = P_\infty - \frac{(P_\infty - P_c)}{\left(1 + \left(\frac{r_d}{2R_0}\right)\right)^{1/2}}, \quad r \leq R_{out}, \quad (4.1)$$

where  $P_c$  and  $P_\infty$  are the central SLP and an estimation of the SLP at an infinite distance, respectively,  $R_{out}$  is the radius of the outermost closed isobar, and  $R_0$  is the radius of the maximum gradient of the SLP. The synthetic SLP field is confined to a circular region specified by  $R_{out}$ . The values of  $P_c$  and  $R_{out}$  can be taken directly from observations recorded by the Tropical Prediction Center (TPC).  $R_0$  is determined from an empirical formula provided by Park and Zou [59],

$$R_0 = 0.38R_{34kt} - 3.8 \quad (4.2)$$

where  $R_{34kt}$  is the averaged 34 kt wind radius (an observed parameter provided by the TPC). The value of  $P_\infty$  can then be estimated by solving Equation 4.1 for  $P_\infty$  and setting  $r_d$  to  $R_{out}$  and  $P_{bogus}$  to  $P_{out}$  ( $P_{out}$  is the pressure of the outermost closed isobar, another TPC observed parameter). Equation 4.1 can then be rewritten as

$$P_\infty = \frac{P_{out}(R_{out})(1 + (R_{out}/R_0^2))^{1/2} - P_c}{((R_{out}/R_0^2) - 1)^{1/2}}. \quad (4.3)$$

The BDA cost function is given by:

$$J = J_{BDA} + J_B \quad (4.4)$$

where,

$$J_{\text{BDA}} = \frac{1}{2} \sum_{r=0,3,6,9,\dots,30\text{min}} (\mathbf{p} - \mathbf{p}^{\text{obs}})^T \mathbf{W} (\mathbf{p} - \mathbf{p}^{\text{obs}}), \quad (4.5)$$

$\mathbf{p}^{\text{obs}}$  is a vector containing the synthetic SLP observations, and  $\mathbf{p}$  is a vector of model pressure from the lowest model level. The weighting matrix  $\mathbf{W}$  is diagonal and  $J_{\text{B}}$  is a background term measuring the difference between the model state vector and the background field. A 4D-Var assimilation of the synthetic SLP is performed in a 30 minute assimilation window. The synthetic SLP is fitted at three minute intervals and remains constant during the assimilation. All model state variables (i.e., pressure, temperature, wind, mixing ratio, etc.) adjust to produce a surface low which is very similar to the synthetic low, while satisfying the dynamical and physical constraint provided by the atmospheric model.

## 4.4 Radiative Transfer Model

The RTM is used to map the state vector of the MM5 atmospheric model to the radiance observation space in order to make comparisons between observations and forecast results. The RTM includes the effects of absorption, emission, single scattering, and multi-scattering, and therefore can be used in precipitating as well as non-precipitating environments. The four-stream approximation of the discrete ordinate method [60] is used to calculate the scattering phase function (determining the contribution from multi-scattering), which is computationally less expensive than higher stream approximations. The radiative transfer equation in a plane-parallel and azimuthally symmetric atmosphere is:

$$\mu \frac{dI_{pl}(\tau, \mu)}{d\tau} = I_{pl}(\tau, \mu) - \frac{\omega_0}{2} \int_{-1}^1 P(\mu, \mu') I_{pl}(\tau, \mu') d\mu' - (1 - \omega_0) B(\tau), \quad (4.6)$$

where  $I_p(\tau, \mu)$  is the radiance at optical depth  $\tau$  ( $\tau = 0$  at the top of the layer) in direction  $\mu$  (the cosine of the zenith angle), the subscript *pl* depicts the orientation of the polarization (horizontal *H*, and vertical *V*),  $\omega_0$  is the albedo for a single scatterer, and  $B(\tau)$  is the Plank function at  $\tau$ .  $B(\tau)$  is expressed as a linear function of  $\tau$ ,  $B(\tau) = B_0 + B_1\tau$  ( $B_0 = B(0)$ ).  $P$  is the scattering phase function which is integrated over all azimuthal directions (approximated by 4 directions in the RTM). The first term on the right hand side of Equation 4.6 is due to absorption and the last term handles emission and single scattering. The multi-scattering contribution (the second term on the right hand side of Equation 4.6) includes the scattering

effects hydrometeors have on radiative transfer. Equation 4.6 is integrated over the depth of the atmosphere to obtain radiance values at the height of the observing satellite.

In a previous study by Amerault and Zou [23], the tangent linear and adjoint models of the RTM were developed and an adjoint sensitivity analysis of the RTM was performed. MM5 model fields were used as input to the RTM to calculate  $T_b$ s. For lower frequency channels, the model-produced  $T_b$ s were realistic when compared to the observations. However, large discrepancies existed between the model-produced  $T_b$ s and the observed  $T_b$ s at 85 GHz. The RTM was producing  $T_b$ s 100 K lower than the lowest SSM/I observed  $T_b$ .

An updated RTM, which includes a mixing formula in the calculation of the dielectric constant for ice particles, produces forecasted  $T_b$ s which are more in line with the observations. Previously, the ice particles and air had been considered a homogeneous mixture with the dielectric constant of the ice particle and the volume of the mixture considered as a solid sphere with the mass of the ice particle. A mixing formula computes a new dielectric constant for the volume mixture which is a function of the dielectric constants of both of the constituents of the mixture. Bohren and Battan [61] chose the Maxwell-Garnett mixing formula for their radar backscattering calculations because it agreed well with observations. More recently, the Maxwell-Garnett mixing formula has been used successfully in Bauer et al. [62] and Skofronick-Jackson et al. [63] to determine the microwave radiometric response to different explicit cloud parameterization schemes. Given the dielectric constants of the main component of the mixture  $\epsilon_0$ , the secondary component  $\epsilon_1$ , and the volume fraction  $v_f$  that the secondary component occupies, the effective dielectric constant given by the Maxwell-Garnett formula is:

$$\epsilon_n = \epsilon_0 \left[ 1.0 + \frac{3v_f \left( \frac{\epsilon_1 - \epsilon_0}{\epsilon_1 + 2\epsilon_0} \right)}{1 - v_f \left( \frac{\epsilon_1 - \epsilon_0}{\epsilon_1 + 2\epsilon_0} \right)} \right]. \quad (4.7)$$

By using the Maxwell-Garnett mixing formula in the RTM, the difference between the lowest observed and forecasted  $T_b$  at 85 GHz was dramatically reduced.

To make the RTM more consistent with the output from the MM5 model and the COAMPS atmospheric model, the RTM now accepts  $q_s$  and  $q_g$  as input, and the values of the intercept parameter  $N_0$  of the drop size distribution and the density  $\rho$  of the hydrometeor are now more consistent with the values of these parameters in the explicit moisture schemes

**Table 4.1.** Values for the intercept parameters used in the RTM based on the explicit moisture scheme used to compute the input.

	R1	R2	GD	SH	COAMPS
$N_{r0}$ ( $\text{cm}^{-4}$ )	0.8	0.8	0.8	0.8	0.8
$N_{s0}$ ( $\text{cm}^{-4}$ )	0.2	0.2	0.03	0.2	0.2
$N_{g0}$ ( $\text{cm}^{-4}$ )	0.04	0.04	0.0004	0.04	0.04
$\rho_r$ ( $\text{g cm}^{-3}$ )	1.0	1.0	1.0	1.0	1.0
$\rho_s$ ( $\text{g cm}^{-3}$ )	0.1	0.1	0.1	0.1	0.1
$\rho_g$ ( $\text{g cm}^{-3}$ )	0.4	0.4	0.913	0.4	0.4

used to create the input of the RTM (Table 4.1). In the case of the R1 and GD schemes, the values of the corresponding intercept and density parameters are identical between the MM5 and the RTM. In the R2 scheme, the intercept parameters are not constant, so the intercept values of the R1 scheme were used in the RTM for the R2 scheme. The R1 intercept and density values were also used for the SH scheme in the RTM because the SH scheme does not use these values. The R1 values will also be used when COAMPS data is used as input to the RTM because the R1 scheme and COAMPS explicit moisture scheme have many common parameters, including intercept and slope values.

Figure 4.1 shows the 85V  $T_b$ s produced from output of a 24 h MM5 forecast (initialized with the BDA scheme) using the GD scheme, as well as the SSM/I observations from the same channel and roughly the same time. Although the position of the lowest  $T_b$ s (indicating areas of microwave scattering by ice particles, in large convective cells) do not coincide in the forecast and observations, the magnitudes of the lowest  $T_b$ s are in much better agreement than in the results of Amerault and Zou [23]. The difference between the lowest  $T_b$ s in the forecast and observations is roughly 20 K, which gives us confidence that the updated RTM is an adequate tool to use for assimilating microwave  $T_b$ s. Much of the remaining difference is due to inability of the forecast model to correctly predict the precipitation fields, which are used as input to the RTM.

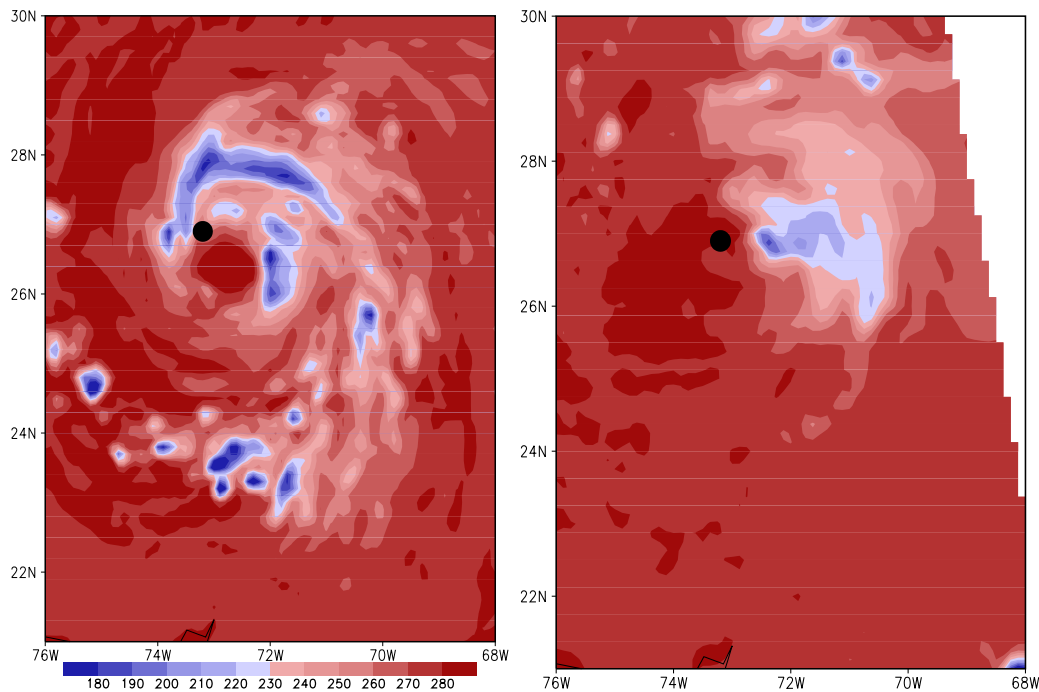


**Figure 4.1.** 85V  $T_b$ s produced by the RTM from a 24 h MM5 forecast using the GD scheme valid 0000 UTC 25 August 1998 (left), and observed 85V SSM/I  $T_b$ s (right) from roughly the same time.  $T_b$ s are in units of K. The filled circles indicates the observed center of Hurricane Bonnie at the forecast time.

## 4.5 Probability Density Functions

To further evaluate the ability of the RTM to produce realistic  $T_b$ s, PDFs were produced for both model-produced and observed  $T_b$ s. The model  $T_b$ s were calculated from MM5 forecasts using the GD, R1, R2, and SH schemes. One 24 h forecast for each of the four explicit moisture schemes and for three different time periods (beginning 1200 UTC 23, 0000 UTC 24, and 1200 UTC 24 August 1998) were conducted. The BDA procedure was performed on a grid with 18 km horizontal spacing (49 x 49 points) and 27 vertical levels to initialize the model. The results of the BDA procedure were then transferred to the forecast grid with smaller horizontal grid spacing (6 km) using bilinear interpolation. The area of the forecast grid was slightly larger than the area of the BDA grid (175 x 205 points in the horizontal domain), but both had the same number of vertical levels.

The Barnes [64] interpolation scheme was used to place the model-produced and observed  $T_b$ s onto domains with the same horizontal grid spacing. The grid spacing was chosen to be representative of the observations because of their coarser resolution compared to the model data. For the 85 GHz channels, the horizontal spacing was 18 km and for all other channels, the spacing was set to 56 km. Not all points in the domain could be used in constructing the PDFs because the observations did not cover the entire domain. For the 85 GHz channels 8612 data points were used to construct the PDFs, for all other channels the number was 1203 because of the greater grid spacing. The SSM/I data fell within a two hour window of the forecast data.

The PDFs for channels 19V, 22V, 37V, and 85V are shown in Figures 4.2. Overall, the PDFs for the different explicit moisture schemes have similar shapes for all channels, and the range covered by the model-produced  $T_b$ s matches well with the range of the observations. However, the peaks of the PDFs don't always match. At 19 GHz (Figure 4.2a), the ocean emits relatively little microwave radiation, so  $T_b$ s in the clear atmosphere will be relatively cold. The warmer temperatures at 19V are due to absorption and emission of radiation by rain drops, which raises the  $T_b$ . The model produces more  $T_b$ s between 230 and 250 K, meaning that the model is producing more rain; however, the difference between the models and observations is not large. Below 230 K the peak in the number of  $T_b$ s is shifted to lower  $T_b$ s for the model when compared to observations.

At 22 GHz (Figure 4.2b) atmospheric water vapor absorbs and emits radiation, which results in a narrow band of  $T_b$ s (most fall between 250 and 270 K). As in the 19V case, most of the  $T_b$ s produced by the model are slightly cooler than the observations.

For the 37V channel (Figure 4.2c), the peaks of the observations and the model data are in the same bins. Radiation at this frequency behaves similarly to the 19V channel except that scattering due to atmospheric ice particles has more of an effect on the radiation which acts to cool the  $T_b$ s. This is difficult to see in the PDFs because of the already relatively low  $T_b$ s which are being emitted by the ocean surface. However, the PDFs for the model data do not show the same uniformity as in the 19V channel which may be due to the differences in the way the different schemes handle ice phase processes.

At 85 GHz (Figure 4.2d), more data points were available to construct the PDFs (8612). Compared to the other channels, the ocean emits much more radiation, so the warmer  $T_b$ s

indicate precipitation-free conditions. The peak in the model data is slightly warmer than the peak in the observations. All the schemes produce more  $T_{bs}$  below 270 K. This is most likely due to an over production of precipitating particles (rain drops for  $T_{bs}$  just below 270 K and snowflakes and graupel pellets for the lowest  $T_{bs}$ ). However, the shape of the PDF fits the observations well considering the amount of uncertainty that exists in the forecasts of precipitating particles by the MM5.

Overall, the model-produced PDFs match the observed PDFs well and are similar between the different explicit moisture schemes. However, at 6 km grid spacing, the upper limit of the resolution of these schemes is being tested. Therefore, we repeated the same three forecasts with 2 km horizontally spaced nests inside the forecast domains. The nests were chosen to be centered around the area of heaviest model-produced precipitation associated with Bonnie at the 24 h forecast time. New PDFs were constructed using only model data from points in the area covered by the nested domains with no interpolation performed. Three different PDFs were constructed using data from i) the 2 km spaced nest (P1), ii) the 6 km spaced domain, which contained the nest, over the area covered by the nest (P2), and iii) the 6 km spaced domain, which did not contain the nest, over the same area as the previous two cases (P3). The new PDFs are shown in Figure 4.3 for 85V  $T_{bs}$  (7803 points were used to construct the P2 and P3 curves and 68403 points were used to construct the P1 curves).

These PDFs show that there is quite a bit a difference between the explicit moisture schemes. The peak of the GD curve is located at 250 K for the P1 and P2 curves and at 265 K for the P3 curve. There is also a secondary peak at 290 K which is larger for P1 and P2 curves than for the P3 curve. For the R1 scheme, the P1, P2, and P3 curves are all similar in shape and value. They peak at 225 K, which is colder than the GD peak, and have a secondary peak at 290 K, similar to the secondary peak in the GD curve. The P1 and P2 curves of the R2 scheme also peak at 225 K, but the peak of the P3 curve is shifted slightly to a warmer 240 K. The secondary peak in the R2 curves is not as pronounced as it is in the GD and R1 curves. Finally, the P1 and P2 curves of the SH scheme have a U-shaped distribution from 210 to 290 K, while the P3 curve has a primary peak at 270 K and a secondary peak at 290 K. The GD and R2 schemes show the most difference between the P1 and P3 curves, while the R1 scheme shows the least. Since the R2 and GD schemes include

more cloud scale processes, we are not surprised to see greater differences compared to the R1 scheme when the model’s resolution is increased.

Although the PDF curves for the different explicit schemes were similar when interpolated to a domain with larger grid spacing, there were a number of differences on smaller spaced domains between the schemes. In the next section we will use the differences between the schemes to estimate the background error associated with the hydrometeors model fields.

## 4.6 Error Estimations

In addition to an accurate observation operator, reliable estimates of the error associated with the background field, the observations, and the observation operator are necessary for a successful assimilation scheme. Full error covariance matrices cannot be stored and are difficult to calculate. Fortunately, the full matrices are not necessary, but good approximations are required for a reliable assimilation process. When assimilating rain-affected microwave  $T_b$ s, most error matrices are usually assumed to be diagonal [65] [20] [21]. For the RTM, Aonashi and Liu [65] assumed that the root mean squared (RMS) forward modeling errors were 5 K for the 85 GHz channels and 3 K for all other channels. Amerault and Zou [23] showed that expected RMS errors of the RTM fell well within these values. A cold bias exists in the RTM when compared to RTMs which have a better representation of the multi-scattering contribution to radiation. This bias is largest in higher frequency channels (85 GHz), but is only on the order of 1 K [23]. The RMS error of the observations has been assumed to be 1 K in previous assimilation experiments [65] [20] and a structure function analysis [23] showed this to be a good estimate. Furthermore, Moreau et al. [21] showed that accounting for correlation between the different observational channels has a marginal impact on the assimilation results.

The background field plays an important role in the assimilation of microwave  $T_b$ s because the model fields encompass a three dimensional space, while the observations are only provided in two dimensions. For instance, at one point, observations from the seven SSM/I channels are available, while the number of model variables at a given point and time in the horizontal plane is on the order of 150-500 (5-10 prognostic variables at 30-50 levels). Therefore, it is important to construct a reasonable approximation to the background error

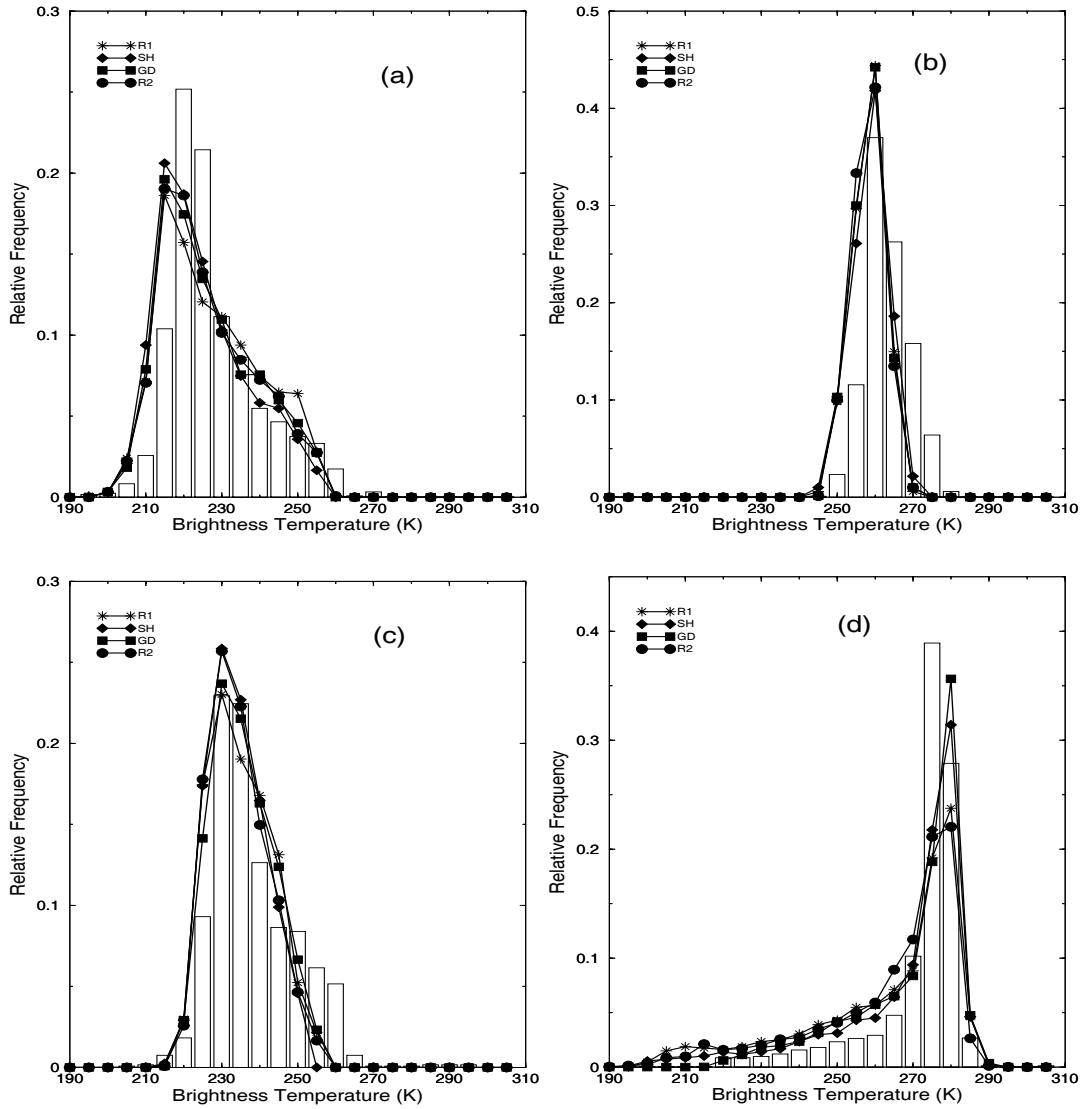


**Figure 4.2.** Relative frequency of occurrence over three forecast domains of (a) 19V, (b) 22V, (c) 37V, and (d) 85V  $T_b$ s. The  $T_b$ s were placed in 5 K intervals, the observations are shown by the bins, while the  $T_b$ s produced by the different explicit moisture schemes are shown as curves (the legend in graph differentiates between the schemes). The  $T_b$ s were interpolated to grids with horizontal spacing of 56 km in (a) - (c) and 18 km in (d).

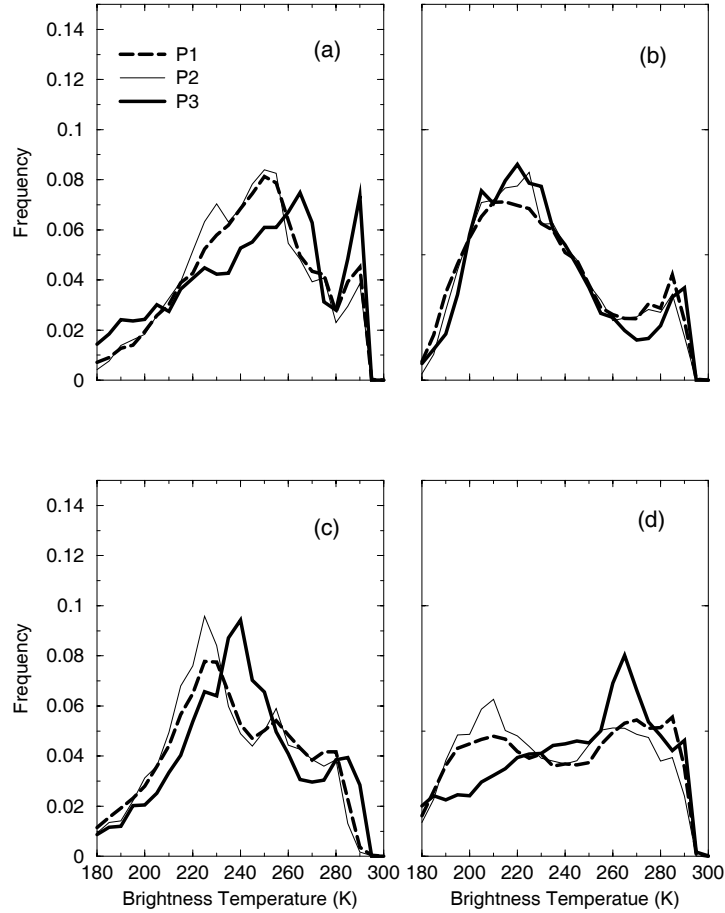


**Figure 4.3.** P1, P2, and P3 relative frequency plots of model-produced 85V  $T_b$ s for the (a) GD, (b) R1, (c) R2, and (d) SH schemes.

covariance so that the proper information is extended to remote locations with an appropriate weighting in the assimilation process.

Some work has been done to define vertical background error covariance matrices for hydrometeors [66] [20], but only values for the liquid states were emphasized. In Moreau et al. [20], the vertical background error covariance matrices were calculated at each forecast point in the horizontal domain of a global model. Profiles of temperature and water vapor were perturbed according to their background error values and used as input for the model's moisture scheme. The resulting profiles of  $q_c$  and  $q_r$  were then used to compute the local background error covariances for each point in the model's horizontal domain. This approach

is not well suited for this study, because a single matrix that can be used at each point is desired and the explicit moisture schemes considered here require profiles of the hydrometeors as well as temperature and water vapor as input.

The National Meteorological Center (NMC) technique [27] is another widely used method for estimating background errors which uses differences between the analysis and forecasts fields valid at the same time to estimate error values. In the case of hydrometeor variables, the analysis values are always zero, so the differences would actually be the forecast values. Here, we will look at an alternative way to define the background error covariance matrices as well as their inverses for all hydrometeor (including frozen) types using differences in model variables from forecasts using different explicit moisture schemes.

For this study, background error covariances are constructed which are non-diagonal in the vertical. To do this, the following steps were utilized. Consider a generic model variable  $d$ , then the element in the  $i$ th row and  $j$ th column of the background error covariance matrix is estimated using

$$d'_{ij} = \overline{(\tilde{d}_{i,p}^{m,n} - \bar{d}_i)(\tilde{d}_{j,p}^{m,n} - \bar{d}_j)}, \quad (4.8)$$

where,

$$i = 1, 2, \dots, K, \quad j = 1, 2, \dots, K, \quad p = 1, 2, \dots, N,$$

$$m = 1, \dots, 4, \quad n = 1, \dots, 4, \quad m \neq n,$$

$$\tilde{d}_i^{m,n} = d_i^m - d_i^n, \quad (4.9)$$

and,

$$\bar{d}_i = \frac{\sum_m \sum_n \sum_p \tilde{d}_{i,p}^{m,n}}{\sum_m \sum_n \sum_p 1}, \quad m \neq n, \quad (4.10)$$

where  $K$  is the number of vertical levels, and  $N$  is total number of points in the horizontal domain used in the calculation. The subscripts  $m$  and  $n$  are used to index the four different explicit moisture schemes discussed in Section 4.1. For the  $p$ th point, the value  $\tilde{d}_i^{m,n}$  is the difference in the variable  $d$  between forecasts using the  $m$ th and  $n$ th explicit moisture schemes at the  $i$ th level, while the average value of  $\tilde{d}_i^{m,n}$  between all combinations of schemes and all points at the  $i$ th level is given by  $\bar{d}_i$ . In the following calculations, all profiles were transferred from the model's sigma coordinate levels to a standard set of 23 height levels covering a range from 0 to 15 km. Furthermore, all calculations were performed at rainy

points. A point was considered rainy if the integrated rainwater value exceeded 1 mm for either profile used to calculate the difference (Equation 4.9).

Estimates of the vertical background error covariance matrix of cloud water  $\mathbf{B}_{q_c}$  are shown in Figure 4.4 using different data sets of Hurricane Bonnie forecasts. The matrices have been decomposed into an error correlation matrix and a profile of the standard deviation of the error. In the first case (C1, Figure 4.4a) the rainy points from the three 24 h forecasts times on the 2 km nests discussed in Section 4.5 were used to construct  $\mathbf{B}_{q_c}$ . For the second case (C2, Figure 4.4b), 1500 points from the more than  $2 \times 10^5$  points used in C1 were randomly chosen to compute  $\mathbf{B}_{q_c}$ . The forecasts from C1 were repeated for the first time period on a domain with 50 vertical levels for the third case (C3, Figure 4.4c). Finally, in the fourth case (C4, Figure 4.4d), the forecasts from C1 were again repeated for the first time period on a domain with 27 vertical levels and a horizontal grid spacing of 18 km.

For each case, the standard deviation of the background error estimate rises from a value of 0.0 at the surface to a maximum of approximately  $0.5 \text{ g kg}^{-1}$  at 4.5 kilometers. The values then decrease and become zero between 12.0 and 13.0 km. The correlation patterns between the different cases are also similar. The highest correlations are along the diagonal. In C1 and C3, the non-zero diagonal values extend up to 13.0 km, while in C2 and C4, the values along the diagonal become zero above 12.0 km. However, at these heights, the standard deviations are more than an order of magnitude less than the maximum values, so the full background error covariance values are relatively small. From this figure, we see that the structure and values of the vertical background error covariance matrices are rather insensitive to the domain grid spacing (both in the horizontal and vertical) and that a relatively small set of profiles can be used to estimate the matrices.

Profiles from 24 h forecasts of a dozen different hurricanes were used to construct the background error covariance of cloud water  $\mathbf{B}_{q_c}$ , cloud ice  $\mathbf{B}_{q_i}$ , rain water  $\mathbf{B}_{q_r}$ , snow  $\mathbf{B}_{q_s}$ , and graupel  $\mathbf{B}_{q_g}$ . The information on the forecast grid configurations and times for the different forecasts is given in Table 4.2. For each hurricane, four 24 h forecasts were run (one for each explicit moisture scheme) and a set of rainy points from the forecast data were randomly chosen to be included in the calculation. The number of points chosen from each hurricane is given in Table 4.2. In the case of Hurricanes Bonnie and Isabel, the data were taken from nests with 2 and  $1\frac{2}{3}$  km horizontal grid spacing, respectively and a larger number of points

were used because the remaining 10 cases all had horizontal spacings which were much larger (15-30 km).

Figure 4.5 shows the estimates of  $\mathbf{B}_{qc}$ ,  $\mathbf{B}_{qi}$ ,  $\mathbf{B}_{qr}$ ,  $\mathbf{B}_{qs}$ , and  $\mathbf{B}_{qg}$  decomposed into error correlation matrices and profiles of the standard deviation of the error. For  $\mathbf{B}_{qc}$  (Figure 4.5a), the correlation structure looks similar to the structures in Figure 4.4. The non-zero element of the diagonal of  $\mathbf{B}_{qi}$  (Figure 4.5b) extend from 5.0 km up to 15.0 km, while the largest standard deviations values are located around 12.0 km. The spread along the diagonal is wider for  $\mathbf{B}_{qr}$  (Figure 4.5c) than for  $\mathbf{B}_{qc}$ . This type of behavior was also observed in the matrices calculated by Moreau et al. [20]. Similarly, the spread along the diagonal for  $\mathbf{B}_{qs}$  (Figure 4.5d) and  $\mathbf{B}_{qg}$  (Figure 4.5e) are both wider than the spread along the diagonal of  $\mathbf{B}_{qi}$ , meaning that the vertical correlation length scale of the background error is larger for precipitating hydrometeors than it is for non-precipitating hydrometeors. The maximum standard deviation for rain water is located around 2.5 km which is below the cloud water maximum. The maximum standard deviation of background error for graupel occurs at 6.0 km while for snow it is at 8.0 km, both of which are below the cloud ice maximum.

For the assimilation procedure, the inverse of these covariance matrices are needed. However, simply inverting these matrices leads to noisy structures which are difficult to physically interpret. Therefore, we first calculated the singular value decomposition (SVD) of the background error covariance matrices and then removed the small singular values before computing the inverse. In SVD, a matrix  $\mathbf{A}$  can be decomposed as

$$\mathbf{A} = \mathbf{U}\mathbf{W}\mathbf{V}^T, \quad (4.11)$$

where in this case  $\mathbf{U}$  is a  $K \times K$  column-orthogonal matrix,  $\mathbf{V}$  is a  $K \times K$  orthogonal matrix, and  $\mathbf{W}$  is a  $K \times K$  diagonal matrix containing the singular values  $w_j$ . Since  $\mathbf{A}$  is a square matrix, its inverse  $\mathbf{A}^{-1}$  can easily be computed using

$$\mathbf{A}^{-1} = \mathbf{V}\tilde{\mathbf{W}}\mathbf{U}^T, \quad (4.12)$$

where  $\tilde{\mathbf{W}}$  is a diagonal matrix containing the values  $\frac{1}{w_j}$  along the diagonal, unless  $w_j$  is zero or small enough to be neglected, then the corresponding value  $\frac{1}{w_j}$  in  $\tilde{\mathbf{W}}$  is set to zero.

The five largest normalized singular values of  $\mathbf{B}_{qc}$ ,  $\mathbf{B}_{qi}$ ,  $\mathbf{B}_{qr}$ ,  $\mathbf{B}_{qs}$ , and  $\mathbf{B}_{qg}$ , are shown in Figure 4.6. The drop-off in value with succeeding singular values is large for all the

hydrometeors, but more so in the case of the precipitating hydrometeors where the second largest singular value is less than 25% of the value of the largest singular value. Only the largest singular value was used in calculating the inverse matrices. Areas of negative values appeared in the inverse matrices if more than 1 singular value was included in the calculation, which is not a desirable feature of a weighting matrix. Figure 4.7 shows estimates of the  $\mathbf{B}_{q_r}$  matrix using only the largest singular value versus using all available values. The two matrices are very similar which means that much of the structure of the full matrix can be captured with only the largest singular value.

The values of  $\mathbf{B}_{q_c}^{-1}$ ,  $\mathbf{B}_{q_i}^{-1}$ ,  $\mathbf{B}_{q_r}^{-1}$ ,  $\mathbf{B}_{q_s}^{-1}$ , and  $\mathbf{B}_{q_g}^{-1}$  are shown in Figure 4.8. These matrices will be used as weightings, so it is important that their structure can be interpreted physically. Using only one singular value, the largest values of  $\mathbf{B}_{q_r}^{-1}$  (Figure 4.8c) are spread out along the diagonal in the lower left portion of the matrix. The weighting for rain water will therefore be greatest in the lower troposphere where rain water amounts are greatest. Positive weightings are also correctly placed in the area of the matrix corresponding to the upper troposphere where graupel and snow concentrations are greatest for  $\mathbf{B}_{q_s}^{-1}$  (Figure 4.8d) and  $\mathbf{B}_{q_g}^{-1}$  (Figure 4.8d), respectively. In the case of the non-precipitating hydrometeors, the values of  $\mathbf{B}_{q_c}^{-1}$  (Figure 4.8a) are greatest in the lower atmosphere and the values of  $\mathbf{B}_{q_i}^{-1}$  (Figure 4.8b) are largest in the upper atmosphere.

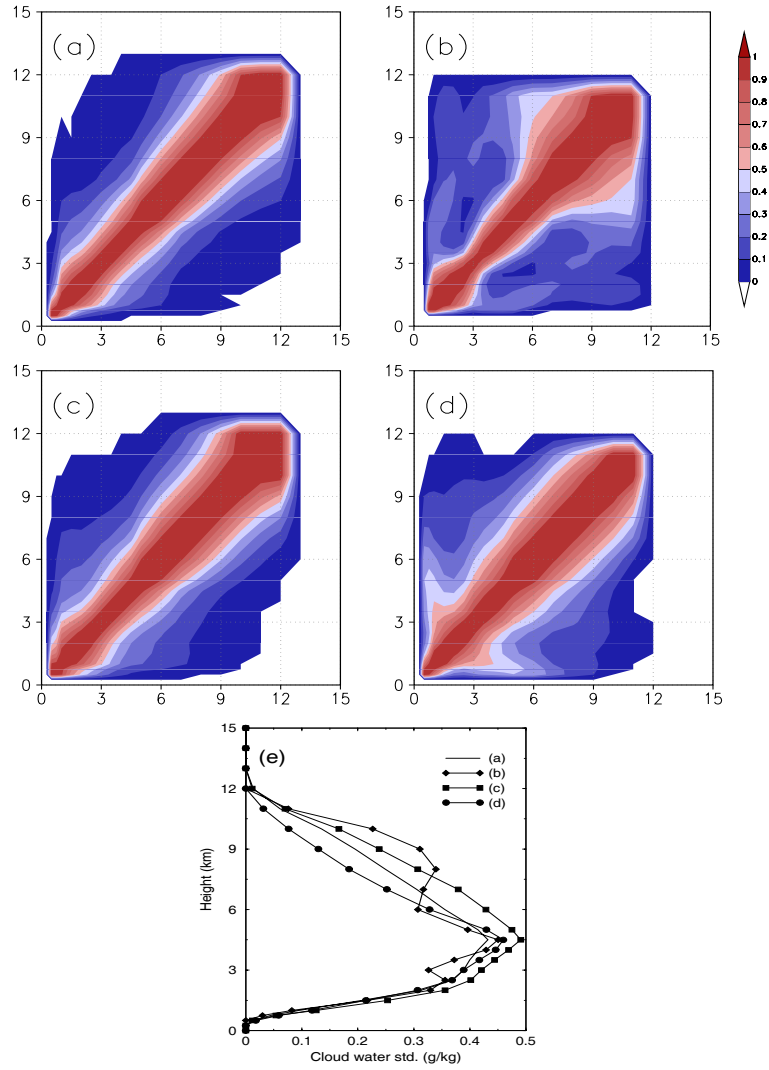


**Figure 4.4.** Vertical background error correlation matrix of  $q_c$  calculated using the data from (a) C1, (b) C2 (c) C3, and (d) C4. The standard deviations of the background error at each level in (a)-(d) are shown in (e). In (a)-(d), the contour interval is 0.2 and the axis labels correspond to height in kilometers.

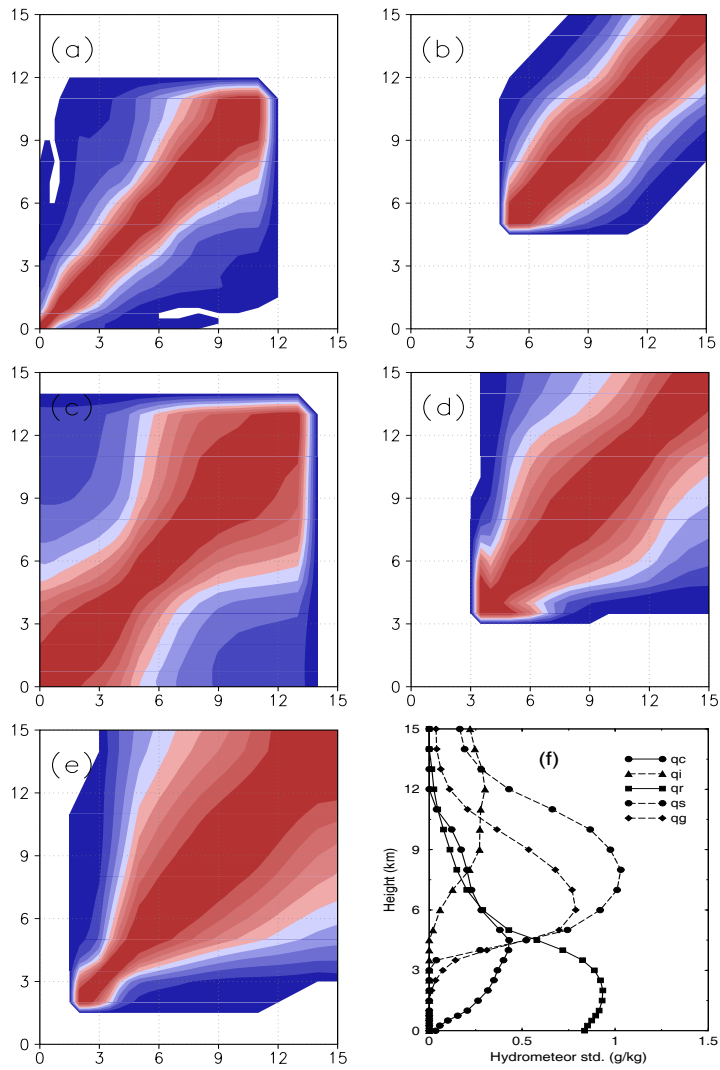


**Figure 4.5.** Vertical background error correlation matrices of (a)  $q_c$ , (b)  $q_i$ , (c)  $q_r$ , (d)  $q_s$ , and (e)  $q_g$  using data from 12 different hurricanes. The standard deviations of the background error at each level in (a)-(e) is shown in (f). In (a)-(d), the contour interval is 0.2 and the axis labels correspond to height in kilometers.

**Table 4.2.** Domain configurations for the hurricane forecasts whose data are used to calculate the background error covariance matrices and number of points from each domain used in the calculation.

Hurricane	Forecast Date	# of Domain Points (x-y-z)	Grid Spacing (km)	# of Points in Covariance Calculation
Bonnie	1200 UTC 08/24/1998	151-151-50	2	1500
Isabel	1200 UTC 09/12/2003	91-91-50	$1\frac{2}{3}$	1500
Gordon	1200 UTC 09/18/2000	111-111-28	18	300
Charley	1200 UTC 08/12/2004	159-167-27	18	300
Erin	1500 UTC 09/09/2001	85-85-27	15	300
Alberto	1500 UTC 08/09/2000	85-85-27	15	300
Edouardo	1200 UTC 08/26/1996	109-109-27	30	300
Irene	1200 UTC 10/16/1999	109-109-27	30	300
Lili	0000 UTC 10/21/1996	109-109-27	30	300
Luis	1200 UTC 09/06/1995	109-109-27	30	300
Marilyn	0000 UTC 09/18/1995	109-109-27	30	300
Roxanne	0000 UTC 10/12/1995	109-109-27	30	300

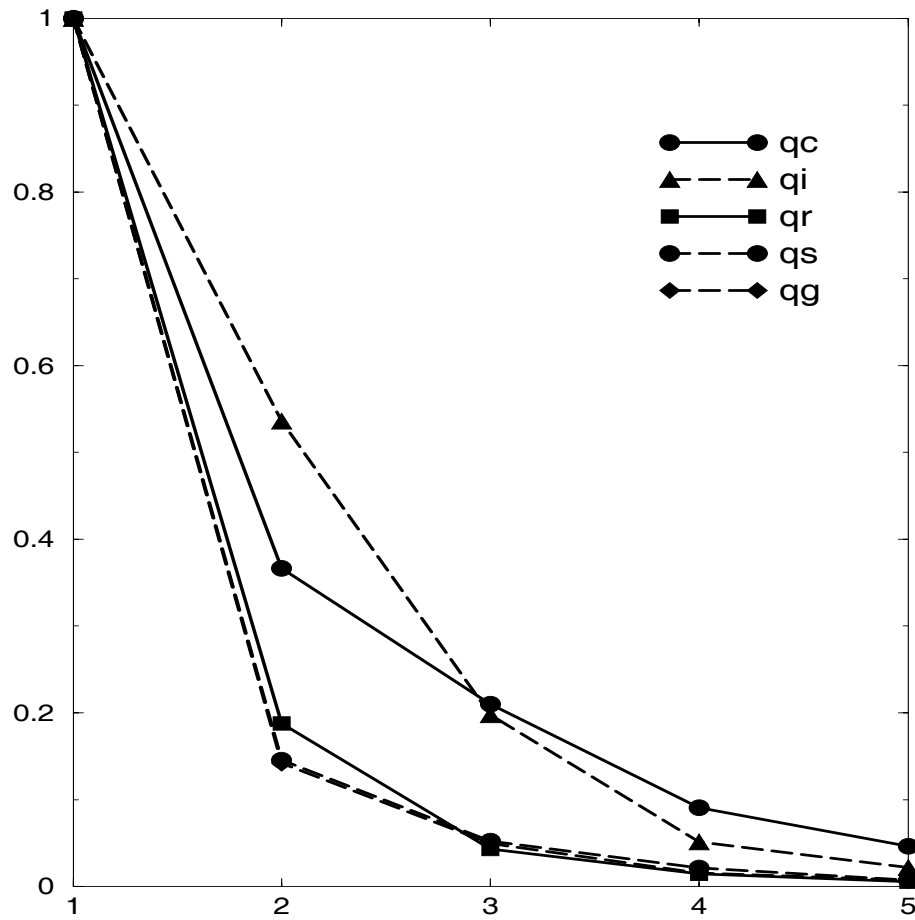


**Figure 4.6.** Normalized singular values (first five ordered from largest to smallest) for the vertical covariance matrices of  $q_c$ ,  $q_i$ ,  $q_r$ ,  $q_s$ , and  $q_g$ .

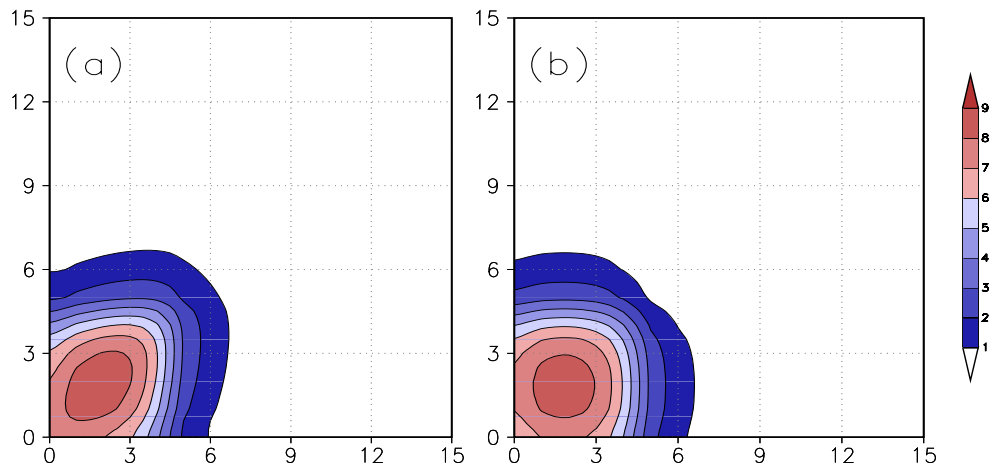


**Figure 4.7.** The full background error covariance matrix of  $q_r$  (multiplied by  $1 \times 10^7$ ) calculated using (a) all available singular values and (b) only the largest singular value. The contour interval is  $1 \text{ kg}^2 \text{ kg}^{-2}$ .

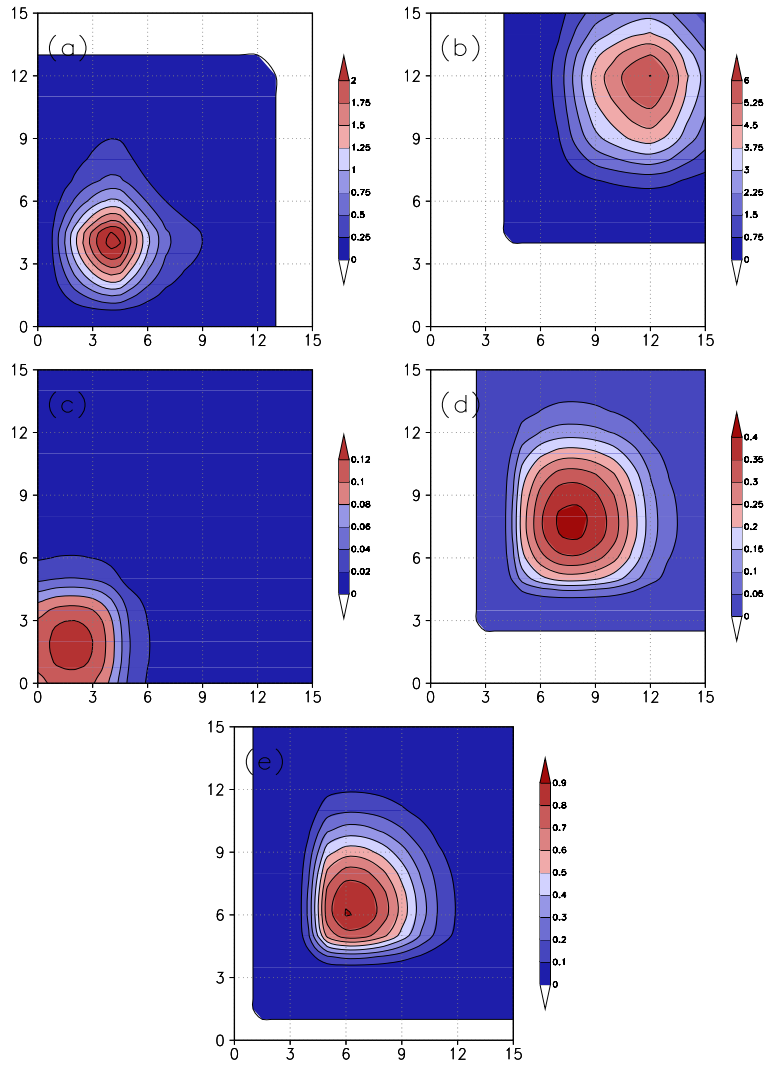


**Figure 4.8.** Inverse the of vertical background error covariance matrix of (a)  $q_c$ , (b)  $q_i$ , (c)  $q_r$ , (e)  $q_s$ , and (e)  $q_g$ . The values have been multiplied by  $1.0 \times 10^{-5}$  and the axis labels correspond to height in kilometers. The contour intervals are (a) 0.25, (b) 0.75, (c) 0.02, (d) 0.05, and (e)  $0.1 \text{ kg}^{-2} \text{ kg}^2$ .

## CHAPTER 5

### ASSIMILATION OF MICROWAVE RADIANCE OBSERVATIONS FOR HURRICANE INITIALIZATION

To this point, we have developed a mesoscale 4D-Var system, which includes an RTM suitable for assimilating rain-affected microwave  $T_b$ s. Here, we will perform some data assimilation experiments involving SSM/I  $T_b$ s to investigate their potential impact on hurricane analyses and forecasts. SSM/I  $T_b$ s are sensitive to atmospheric hydrometeor contents, so it is believed that the assimilation of these observations will improve the initial analysis of precipitation, but it is unclear what effect this will have on the track and intensity forecasts of the hurricane.

#### 5.1 Assimilating Brightness Temperatures

As in Chapter 4, we again focused on Hurricane Bonnie (1998). The COAMPS-AMS was used for both assimilation and forecast experiments. Analyses were produced for 1200 UTC 23 August 1998. The model's domain included 30 vertical levels and 49x49 points in the horizontal with 30 km grid spacing (chosen to be between the resolution of the 85 GHz and lower frequency SSM/I  $T_b$ s). All assimilation and forecast experiments were run on the same domain. A control forecast (CNTRL) was run to compare with the forecasts run from the analyses resulting from the assimilation experiments.

In the first data assimilation experiment (ETB), only microwave radiances were assimilated. The cost function for ETB was defined as:

$$J = J_{TB} + J_B \tag{5.1}$$

where,

$$J_{\text{TB}} = \frac{1}{2} \sum_{r=0,15,\dots,30\text{min}} (\mathbf{T}_{\mathbf{b}}^{\text{RTM}} - \mathbf{T}_{\mathbf{b}}^{\text{obs}})^T \mathbf{W} (\mathbf{T}_{\mathbf{b}}^{\text{RTM}} - \mathbf{T}_{\mathbf{b}}^{\text{obs}}), \quad (5.2)$$

$\mathbf{T}_{\mathbf{b}}^{\text{RTM}}$  is a vector containing the  $T_b$ s calculated by the RTM using the model state vector  $\mathbf{x}$  as input, and  $\mathbf{T}_{\mathbf{b}}^{\text{obs}}$  are SSM/I observations (Chapter 4.2). As in the BDA scheme,  $J_{\text{B}}$  is a background term which serves as an added constraint, which keeps the problem well posed. The background error covariance matrices computed in Chapter 4 were utilized in the assimilation process. The COAMPS analysis field serves as the background and the initial guess of  $\mathbf{x}$ . The weighting matrix  $\mathbf{W}$  is diagonal with elements that are set equal to the estimates of the square of the inverse root mean squared observational error for each of the channels (3 K for the 19, 22, and 37 GHz channels and 5 K for the 85 GHz channels [65]). Only observations from the vertically polarized channels were assimilated because these channels are less sensitive to surface properties and more sensitive to atmospheric variables when compared to the horizontally polarized channels. Observations were only available for one time period over the domain, but as is done in the BDA procedure, the same observational field was used over a short assimilation window and it was assumed to remain constant. In this case, the same SSM/I observations were assimilated at 0, 15, and 30 min.

Figure 5.1 shows the normalized cost function values for 19V, 22V, 37V, and 85V at each iteration of the minimization in ETB. The cost function value is reduced by more than 60% in all cases, although more reduction occurs in the 19V and 37V channels than in the 22V and 85V channels. Here, we will compare the SSM/I observed values to the model-produced  $T_b$ s calculated from the CNTRL and ETB analyses to see how well the assimilation procedure is performing.

At 19V (Figure 5.2), there is a large area of relatively high  $T_b$ s (270 -280 K) associated with the precipitation to the east of the center of Hurricane Bonnie. The CNTRL analysis contains no hydrometeor values so the 19V  $T_b$ s calculated from this field are all relatively low (220-240 K) surrounding the storm. After the assimilation of the SSM/I  $T_b$ s, the analysis field is able to produce high  $T_b$ s on the eastern side of the storm. Figure 5.3 shows the ETB analysis of  $q_r$  at model level  $k = 15$  (approximately 5 km). The maximum values of  $q_r$  are located on the eastern side of the storm and coincide with the area of the maximum 19V

$T_b$ s, which means the improved analysis of 19V  $T_b$ s surrounding the hurricane is due to the production of  $q_r$  by the assimilation of SSM/I  $T_b$ s.

At 22V (Figure 5.4), the highest  $T_b$ s (270-280 K) due to the emission of radiation by  $q_v$  surround the center of the storm and are also located in a band to the north of the storm. In the CNTRL analysis, there is also an area of high  $T_b$ s surrounding the center which are similar in value to the observations, but the band to the north of the storm seen in the observations are not present in the analysis. The differences between the observations and the CNTRL analysis  $T_b$ s at this channel are much less than in the 19V case because the analysis has a better initial representation of  $q_v$  than of  $q_r$  (which is non-existent in the analysis). Since the difference between the analysis and observations at this channel are less than at any other channel, the contribution to the cost function for this channel is much less than the other channels. This is a reason why there is not as much relative decrease in the cost function for this channel when compared to the channels which are sensitive to  $q_r$  (19V and 37V). After the assimilation of SSM/I  $T_b$ s, the ETB analysis of 22V  $T_b$ s was able to capture the band of high  $T_b$ s seen in the observations which was located to the north of the storm.

Just as with the 19V  $T_b$ s, the 37V  $T_b$ s are relatively higher in areas of precipitation over the ocean surface when compared to non-rainy areas. In the 37V observations (Figure 5.5), the highest  $T_b$ s (260-270K) are located in the same areas as they are in the 19V observations. Since there is no precipitation in the CNTRL analysis, the highest 37V  $T_b$ s calculated from the analysis are in the 240-250 K range. In the ETB analysis, an area of  $T_b$ s in the 260-270 K range similar to what is seen in the observations is created due to the creation of  $q_r$  in the analysis fields.

For the 85V  $T_b$ s, the emission coming from the ocean surface is greater than for the other channels, so the  $T_b$ s in non-rainy areas are relatively larger (270-280 K). In areas of precipitation, the  $T_b$  is relatively lower due to scattering by frozen hydrometeors. In the 85V observations (Figure 5.6), relatively lower values are located to the east of the storm center (210-230 K), but the control analysis has relatively high  $T_b$ s everywhere due to the lack of precipitation fields. The assimilation procedure does produce frozen hydrometeors to the east of the storm (Figure 5.7), but as was seen in Figure 5.1, the  $T_b$  assimilation procedure did not do as well in reducing the portion of the cost function due to the 85V  $T_b$ s when

compared to the other channels. While the lowest ETB values to the east of the storm's center are lower than the CNTRL analysis by 30-40 K, they are still 20 K higher than the observations, which means that the frozen hydrometeors contents in the ETB analysis are not as large as what would have been observed at that time. More work will be required to determine if the  $T_b$  assimilation procedure can produce higher frequency  $T_b$ s which are sensitive to frozen hydrometeors that match the observations as well as the lower frequency  $T_b$ s which are sensitive to liquid hydrometeors. The assimilation procedure may need to be run at a resolution high enough so that the cumulus scheme can be turned off and the deep convection can be explicitly resolved, which would lead to a better representation of the frozen hydrometeors in the model. Overall though, the assimilation of microwave  $T_b$ s is able to produce an analysis field with precipitation hydrometeor values located in the proper location that produce realistic radiance values.

To investigate the effect the hydrometeor background error covariance matrices have on the resulting precipitation fields, another experiment (ETBNBG) was conducted which was identical to ETB except that  $\mathbf{B}_{q_c}$ ,  $\mathbf{B}_{q_i}$ ,  $\mathbf{B}_{q_r}$ ,  $\mathbf{B}_{q_s}$ ,  $\mathbf{B}_{q_g}$ , and their respective inverses were all diagonal. The elements for the diagonal matrices were determined in the same manner as they are for the non-hydrometeor matrices (Chapter 3.4). A vertical cross section of the analysis values of  $q_r$  for ETB and ETBNBG is shown in Figure 5.8. The location of the cross section runs through the center of the storm and is indicated by the line in upper right hand panel of Figure 5.2. The maximum values of  $q_r$  in the vertical are located around 5 km for ETB. For ETBNBG, the maximum  $q_r$  values are dispersed in the vertical along the cross section. At  $71^\circ\text{W}$  and  $69^\circ\text{W}$  the maximum  $q_r$  values are located near 3 km, but between these two locations, the maximum  $q_r$  values rise to 5 km at  $70^\circ\text{W}$ . Even with these different structures in the  $q_r$  field, the ETB and ETBNBG analyses show about the same level of improvement over the CNTRL analysis in radiance space (Figure 5.9). The differences between the 19V SSM/I  $T_b$ s and the analysis values in ETB and ETBNBG along the cross section (5-10 K) are significantly smaller than the differences between the observations and the CNTRL (as large as 45 K). The benefit of using the non-diagonal background error covariance matrices can be seen by looking at profiles at an individual point. Normalized profiles from the  $q_r$  analysis of ETB and ETBNBG at  $24.3^\circ\text{N}$   $69.0^\circ\text{W}$  are shown in Figure 5.10. As was seen in the cross section, there is a single peak in the ETB

$q_r$  profile at 5 km, but there are 2 peaks in the ETBNBG profile (a maximum at 3 km and a secondary peak at 5 km). The profile of the background error correlation for  $q_r$  at 5 km is also shown in Figure 5.10. The correlation values decrease smoothly away from 5 km both above and below and there are no secondary peaks. This analysis has shown that by adding the extra constraint of the vertical correlation present in the background error covariance matrices for the hydrometeor variables, we are able to obtain suitable error reduction in radiance space with realistic hydrometeor profiles.

For the forecast, the assimilation of  $T_{bs}$  in this framework does show some positive impacts. The initial maximum surface windspeed in ETB is over  $50 \text{ m s}^{-1}$  and is much stronger and closer to the observations than the CNTRL value (Figure 5.11). However, this does not correspond to a lower minimum central SLP value in the ETB analysis when compared to the CNTRL analysis. The model is unable to sustain the strong initial windspeed and by 3 h the ETB and CNTRL windspeed are much closer in value, although the ETB maximum windspeed remains larger and closer to the observations. For the minimum central SLP, both the ETB and CNTRL values drop substantially (over 20 hPa) over the initial 24 forecast period, but the ETB value is always 2-3 hPa lower than the CNTRL value and is closer to the observations. The track forecasts of ETB and CNTRL remain within a grid point of each other during the forecast, but both forecasts move the storm too quickly to the northwest and aren't originally placed in the correct location.

We have seen that the assimilation of  $T_{bs}$  is able to create positive hydrometeor concentrations in the resulting analysis. To see if the model was able to retain this information in the forecast, the time evolution of the  $q_r$  field was investigated. Figure 5.13 shows the average  $q_r$  value for ETB and CNTRL at each forecast hour at model level  $k = 15$  (approximately 5 km) in a box  $150 \text{ km} \times 150 \text{ km}$  which remains in the same position relative to the storm's center on the eastern side of the hurricane. This area and model level were chosen because the  $q_r$  concentrations are relatively larger at this height and in this area with respect to the rest of the model's domain. At the initial time, the average ETB  $q_r$  value is  $0.16 \text{ g kg}^{-1}$  which is within the range of values at later forecast times. This gives us confidence that the assimilation of  $T_{bs}$  is leading to realistic hydrometeor concentrations in the analysis field. However, the model is unable to sustain these initial fields and by the first hour, the average  $q_r$  value has fallen to be barely larger than the CNTRL value which

began with no precipitation in the analysis. By the second hour, the ETB and CNTRL average  $q_r$  values have risen to a value just below  $0.10 \text{ g kg}^{-1}$ . As the forecast progresses, the average  $q_r$  values fluctuate between  $0.10$  and  $0.30 \text{ g kg}^{-1}$  for both ETB and CNTRL. From this analysis, it appears that the assimilation window will need to be lengthened (to 3-6 h) in order to sustain the hydrometeor fields created in the analysis by the assimilation of  $T_b$ s.

In radiance space at 19V, there is little difference between the CNTRL and ETB forecast at 24 h after the CNTRL forecast has been able to create precipitation fields (Figure 5.14). Both forecasts show an area of relatively high  $T_b$ s (260-270 K) on the eastern side of the storm. The observation at this channel also show an area of higher  $T_b$ s on the eastern side of the storm, although the maximum values are 10 K higher than the largest values in either the ETB or CNTRL forecasts. At 85V (Figure 5.15), there are more noticeable differences between the ETB and CNTRL forecasts. In the ETB forecast, an area of lower  $T_b$ s extends from the northern side of the storm to the eastern side in a comma shape which is similar to the pattern of lower  $T_b$ s seen in the observations. In the CNTRL forecast, the lowest  $T_b$ s to the north of the storm extend eastward and do not wrap around the storm. Both the ETB and CNTRL forecasts show an area of relatively low  $T_b$ s on the southern side of the storm which is not evident in the observations. From this single case and in this framework, it is difficult to conclude how much of an impact the assimilation of rain-affected  $T_b$ s has on the forecast, but it does seem to create a slightly stronger vortex. In the next section, we will include a synthetic SLP field in the assimilation process to see if we can make further improvements to the forecast.

## 5.2 Assimilating Synthetic SLP and Brightness Temperatures

Here, we will look to see if  $T_b$ s can be combined with the synthetic SLP field used in the BDA procedure to improve hurricane track and intensity forecasts and add value to the forecasts compared to when only the BDA procedure is used. In the first experiment (EBDA), only the synthetic SLP field is assimilated at 3 m intervals over a 30 m window. In the second experiment (E BOTH), the SSM/I  $T_b$ s are assimilated every 15 min and the synthetic SLP field is again assimilated every 3 min over the 30 m window. The grid configuration (49x49x30 points, 30 km horizontal grid spacing) used in the previous experiments was used here.

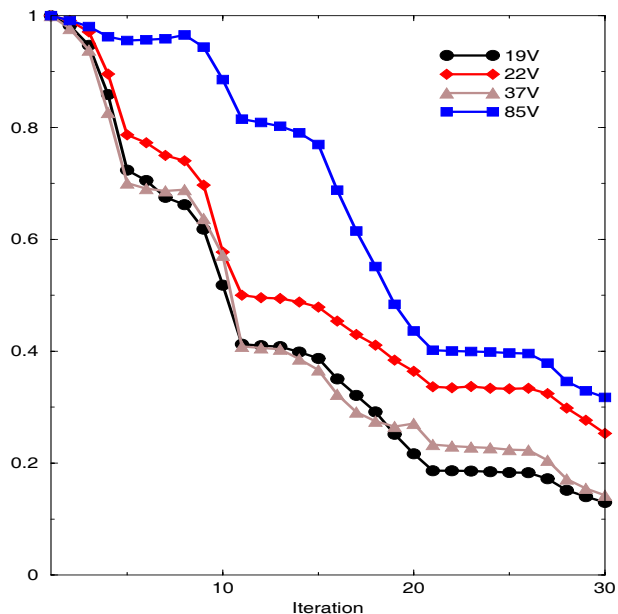


**Figure 5.1.** Normalized value of the cost function for each channel (19V, 22V, 37V, and 85V) at each iteration of the minimization in ETB. The values were normalized by dividing by the respective initial value.

Figures 5.16 and 5.17 are similar to Figures 5.11 and 5.12, respectively, except that the forecasts of EBDA and EBOOTH have replaced ETB and CNTRL. The initial minimum central SLP for EBDA and EBOOTH matches the observed value since the assimilation procedure has fit the initial state to the synthetic SLP field which has a minimum central SLP value equal to the observed value. In EBDA, the initial maximum wind speed is much weaker than the observed value, but in EBOOTH this value is larger and much closer to the observed value due to the assimilation of  $T_b$ s. However, the model is unable to sustain the strong wind in EBOOTH and drops about  $10 \text{ m s}^{-1}$  below the observed value. In EBDA, the windspeed increases during the early forecast period to a value which is slightly less than the value in EBOOTH. For the minimum central SLP, both forecasts are within 5-10 hPa of the observed value during the 24 h forecast period. As is indicated by the stronger winds, EBOOTH also has lower central SLP values (by 2-3 hPa) during the forecast period. This effect of the assimilation of  $T_b$ s was also seen in the previous experiments where the forecast of the ETB storm was slightly stronger than the forecast of the CNTRL storm. The EBDA

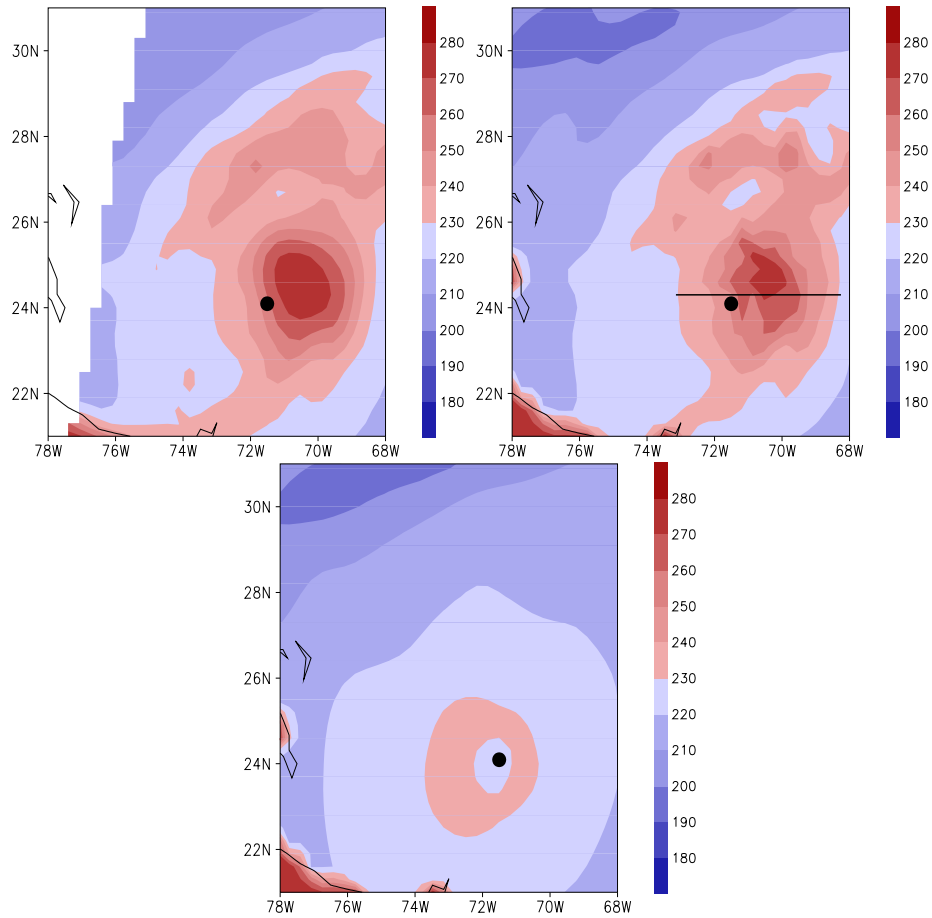


**Figure 5.2.** 19V  $T_b$ s from SSM/I observations (upper left), model-produced from the ETB analysis (upper right), and model-produced from the CNTRL analysis (bottom) at 12 UTC 23 August 1998 in units of K. The filled circles represents the observed center of Hurricane Bonnie, and the line in the upper left panel indicates the location of the cross section shown in Figures 5.8-5.9.

and E BOTH tracks are similar to one another and both are east of the ETB and CNTRL tracks which puts them more inline with the observed track. However, both forecasts move the storm at a faster rate to the northwest than what was observed.

In radiance space, we again see that the assimilation of  $T_b$ s has the greatest impact on the analysis for the lower frequency  $T_b$ s. The 19V EBDA  $T_b$ s (Figure 5.18) are slightly higher at the initial than in the case of the CNTRL analysis, but are still much lower than the observations on the eastern side of the storm. After the assimilation of  $T_b$ s in E BOTH, the

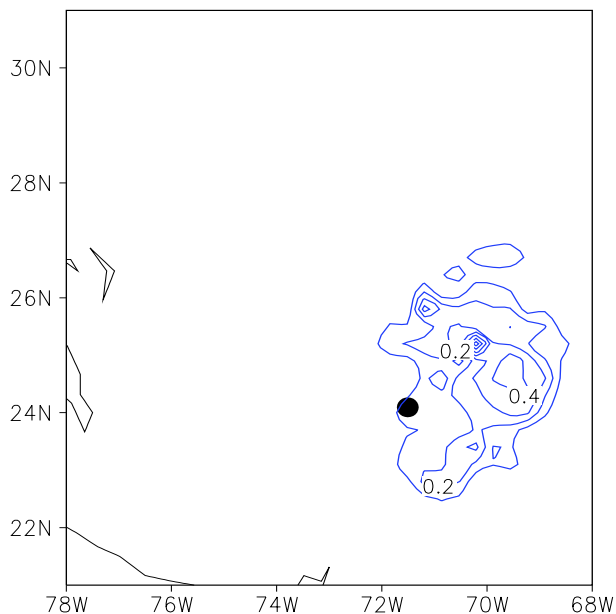


**Figure 5.3.** Initial analysis of  $q_r$  (left) at  $k = 15$  (approximately 5000 m) The contour interval is  $0.1 \text{ g kg}^{-1}$ . and the filled circle indicates the observed center of Hurricane Bonnie.

19V  $T_b$ s look much more like the observed values. At 85V, the EBDA  $T_b$ s (Figure 5.19) are similar to the CNTRL  $T_b$ s (both are relatively high everywhere). In the EBOOTH analysis, the  $T_b$ s on the eastern side of the storm are slightly lower than in the EBDA case, but are still over 30 K higher than lower values seen in the observations and do not match the observations as well as the 19V  $T_b$ s.

For the forecasts in radiance space, there does appear to be a larger difference between EBDA and EBOOTH than was evident in ETB and CNTRL. At 24 h, the largest EBDA 19V  $T_b$ s (Figure 5.20) are located on the northern side of the storm; however, the largest 19V  $T_b$ s are shifted more to the eastern side of the storm which is more consistent with what was seen in the observations. For the 85V EBDA  $T_b$ s (Figure 5.21), the lowest values are located on the southern side of the storm. In the EBOOTH, there is an area of relatively low 85V  $T_b$ s on the northern side of the storm that wraps around to the eastern side and is consistent with what is seen in the observations. However, there is also an area of lower  $T_b$ s on the southern side of the hurricane similar to what is seen in the EBDA 85V  $T_b$ s which is not present in the observations.

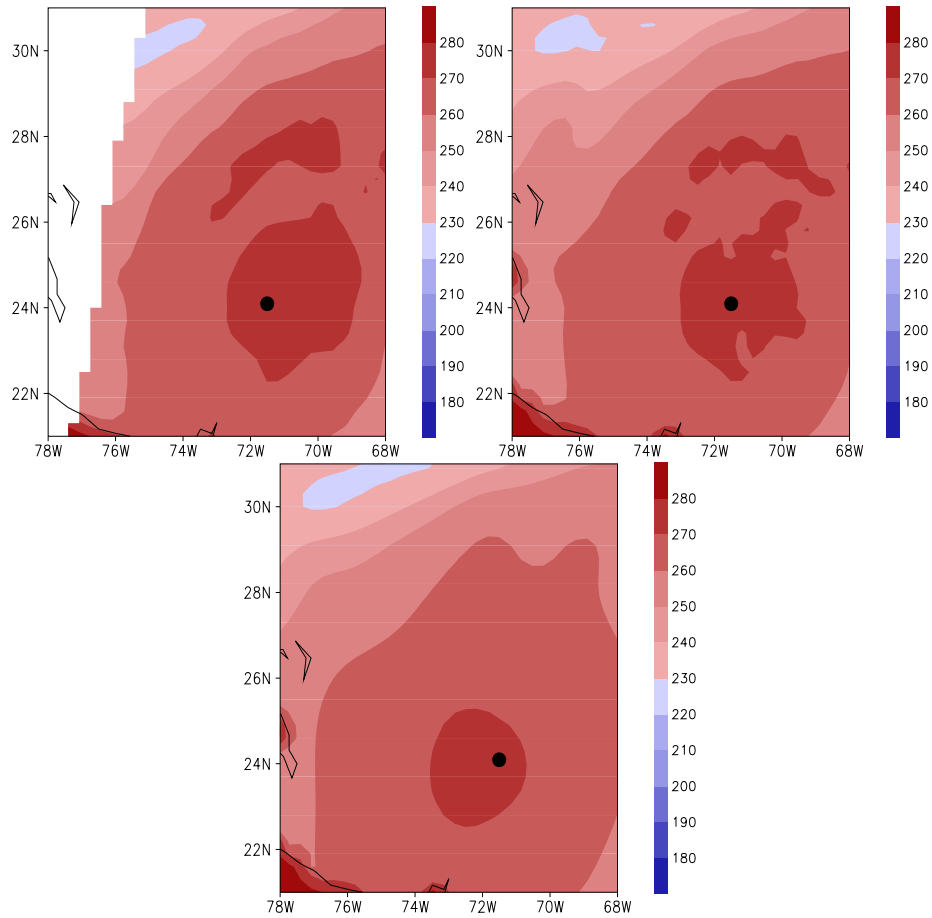


**Figure 5.4.** Same as Figure 5.2 except for 22V  $T_b$ s.

Again, from just one case it is difficult to conclude how much of an impact the assimilation of rain-affected  $T_b$ s has on the forecast, but it does seem to hold promise for improving hurricane analyses and forecast. After the assimilation of  $T_b$ s, the analysis in radiance space for the lower frequency  $T_b$ s matched the observations well due to the production of hydrometeors, but more work is needed to see the same level of improvement for the higher frequency  $T_b$ s which are sensitive to frozen hydrometeors. The assimilation process produced maximum surface windspeeds associated with a hurricane which were close to the observed values. However, the model was unable to sustain these strong winds in the integration. This is area which also needs further testing to improve the way the information contained in the analysis impacts the forecast. Now that we have shown that rain affected  $T_b$ s are

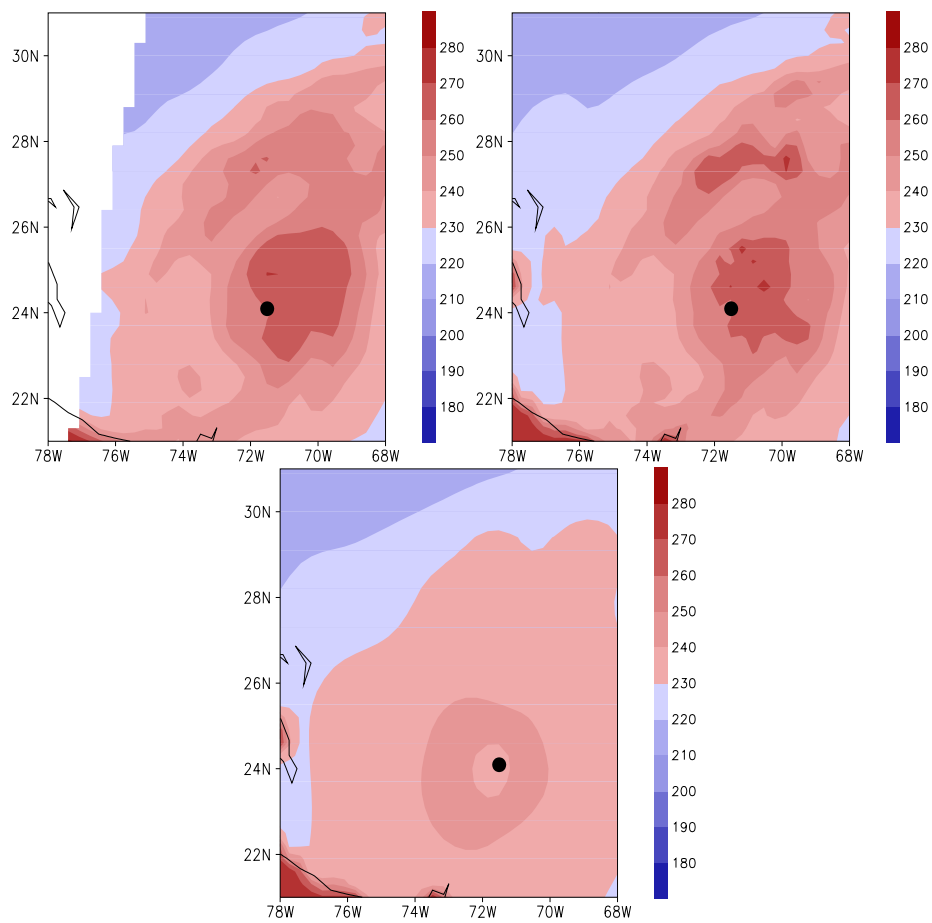


**Figure 5.5.** Same as Figure 5.4 except for 37V  $T_b$ s.

capable of being assimilated in this system, we can focus our future efforts on maximizing forecast impact of the information gained during the assimilation process.

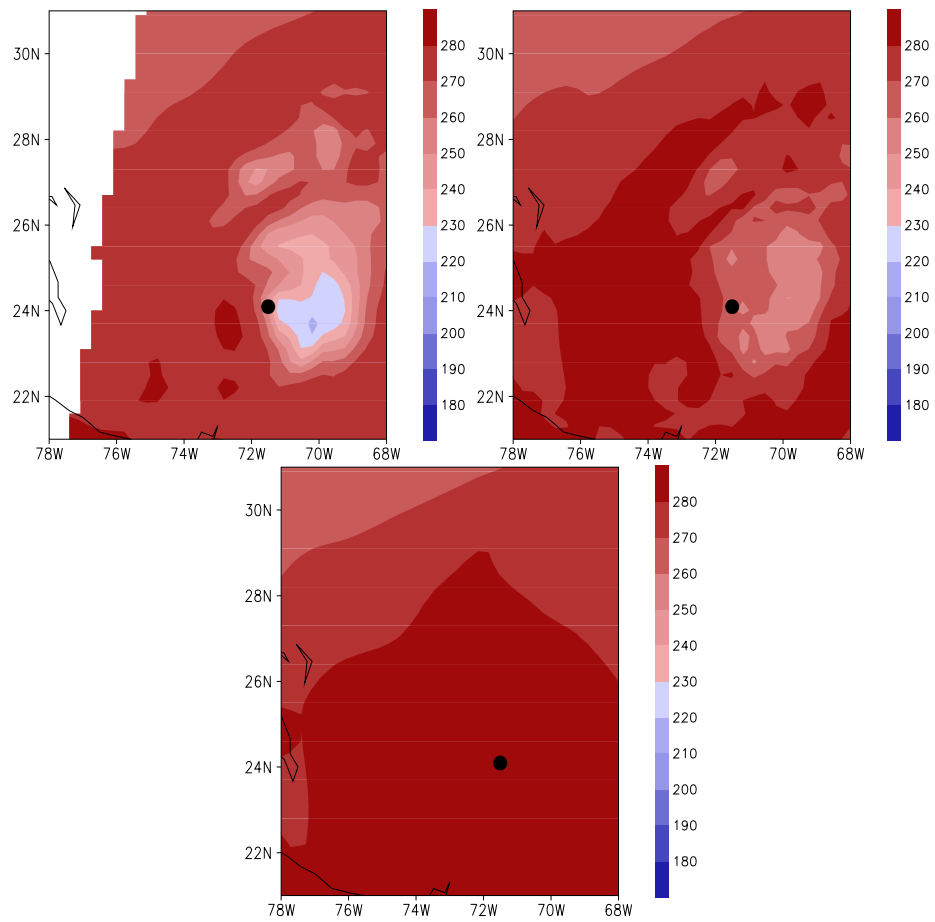


**Figure 5.6.** Same as Figure 5.5 except for 85V  $T_b$ s.

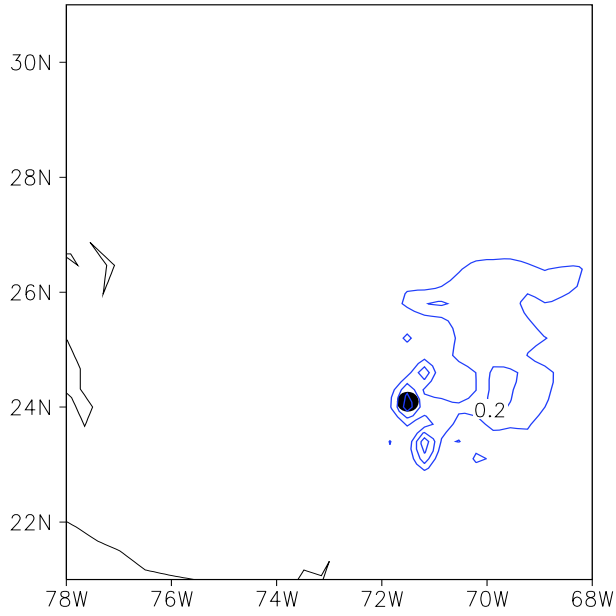


**Figure 5.7.** Same as figure 5.3 except for  $q_s$  at model level  $k = 12$  (approximately 8000 m).

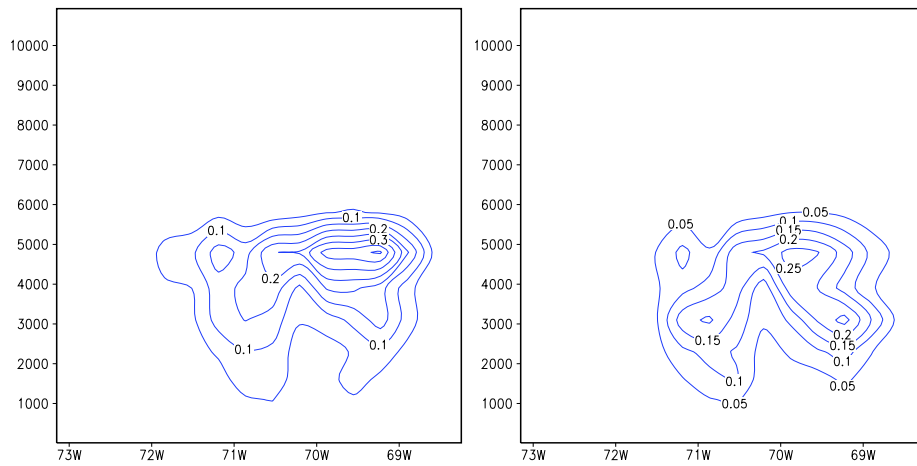


**Figure 5.8.** Vertical cross section of  $q_r$  analysis values for ETB (left) and ETBNBG (right) at  $24.3^\circ$  N. The contour interval is  $0.1 \text{ g kg}^{-1}$  and the labels on the  $z$ -axis refer to the height in m. The location of the cross section is indicated by the line in Figure 5.2.

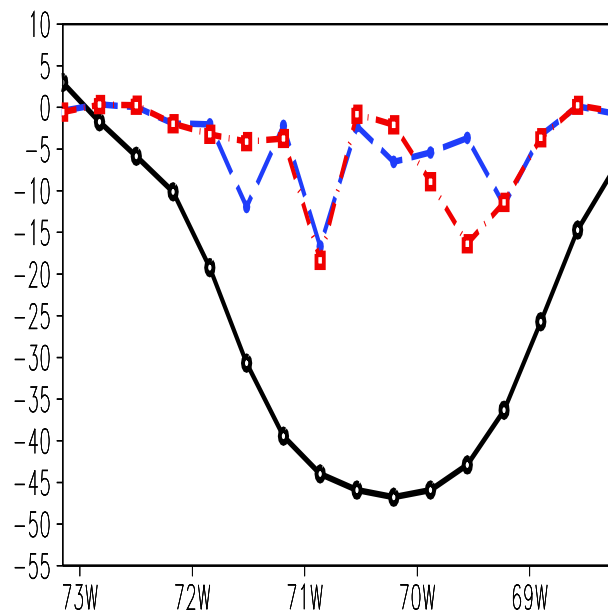


**Figure 5.9.** Difference between 19V  $T_{bs}$  from the SSM/I observations and the CNTRL analysis (CNTRL-SSM/I, black line), SSM/I observations and the ETB analysis, (ETB-SSM/I, blue dashed line), and SSM/I observations and the ETBNBG analysis (ETBNBG-SSM/I, red dot-dashed line) along the cross section at  $24.3^\circ$  N show in Figure 5.2. The  $y$ -axis denotes the difference values in K.

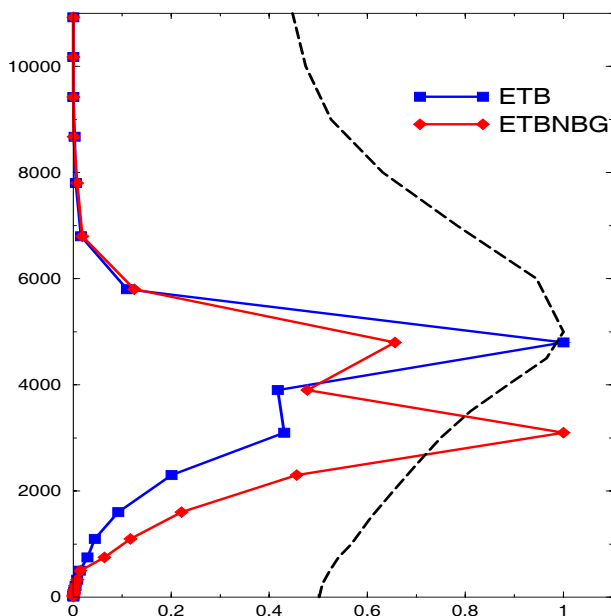


**Figure 5.10.** Normalized profiles of the analysis values of  $q_r$  for ETB (blue squares) and ETBNBG (red diamond) at  $24.3^\circ\text{N}$  and  $69.0^\circ\text{W}$ . The profiles were normalized by the largest value in the respective profile. The black dashed line is a profile of the correlation at 5 km in the  $\mathbf{B}_{q_r}$  matrix shown in Figure 4.5. The labels on the  $z$ -axis refer to the height in m.

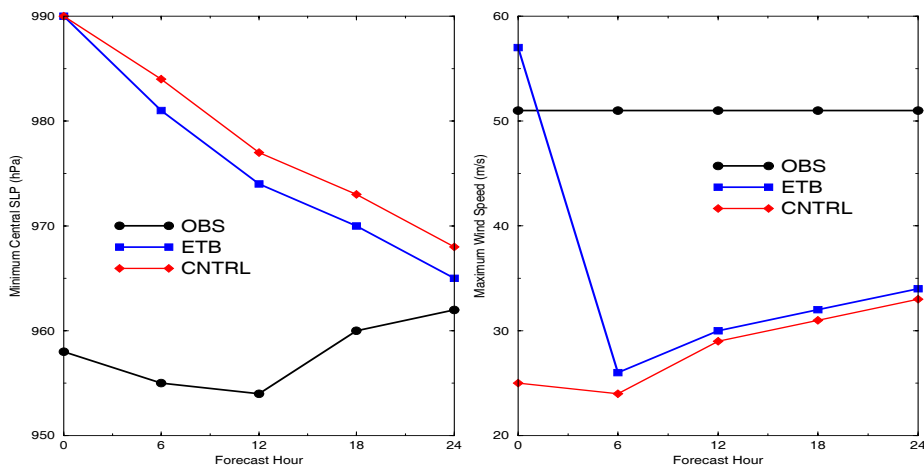


**Figure 5.11.** Observed and forecasted minimum central SLP (left) and maximum surface wind speed (right) from ETB and CNTRL of Hurricane Bonnie for the 24 h period beginning 1200 UTC 23 August 1998. Units are in hPa (left) and  $\text{m s}^{-1}$ .

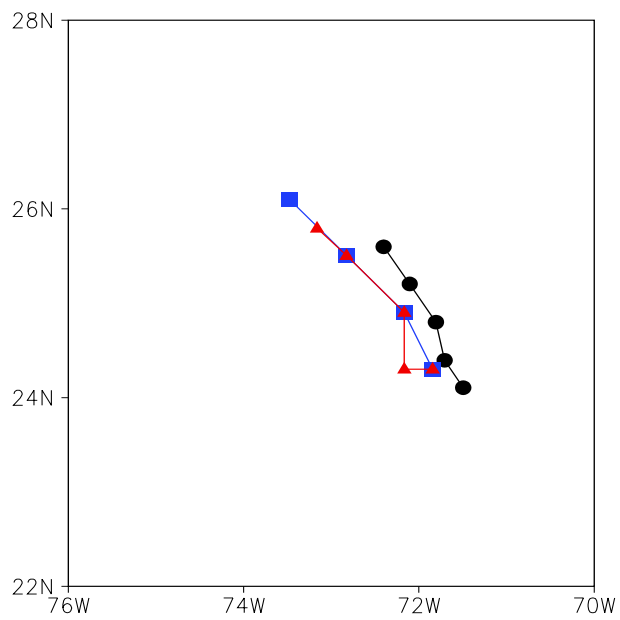


**Figure 5.12.** Observed (black circles) and forecasted track from ETB (blue squares) and CNTRL (red triangles) of Hurricane Bonnie for the 24 h period beginning 1200 UTC 23 August 1998.

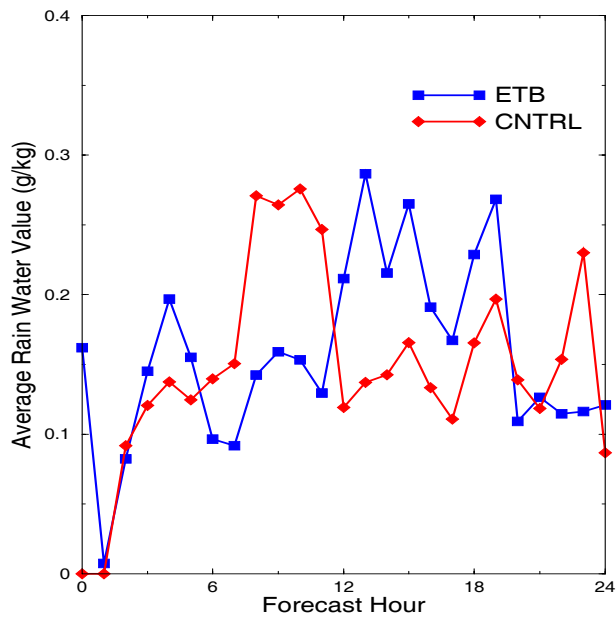


**Figure 5.13.** Averaged value of  $q_r$  for ETB and CNTRL for the 24 h forecasts at model level  $k = 15$  (approximately 5 km) in a  $150 \text{ km} \times 150 \text{ km}$  box on the eastern side of the storm. The box was positioned on the eastern side of the hurricane always at the same position relative to the storm's center.

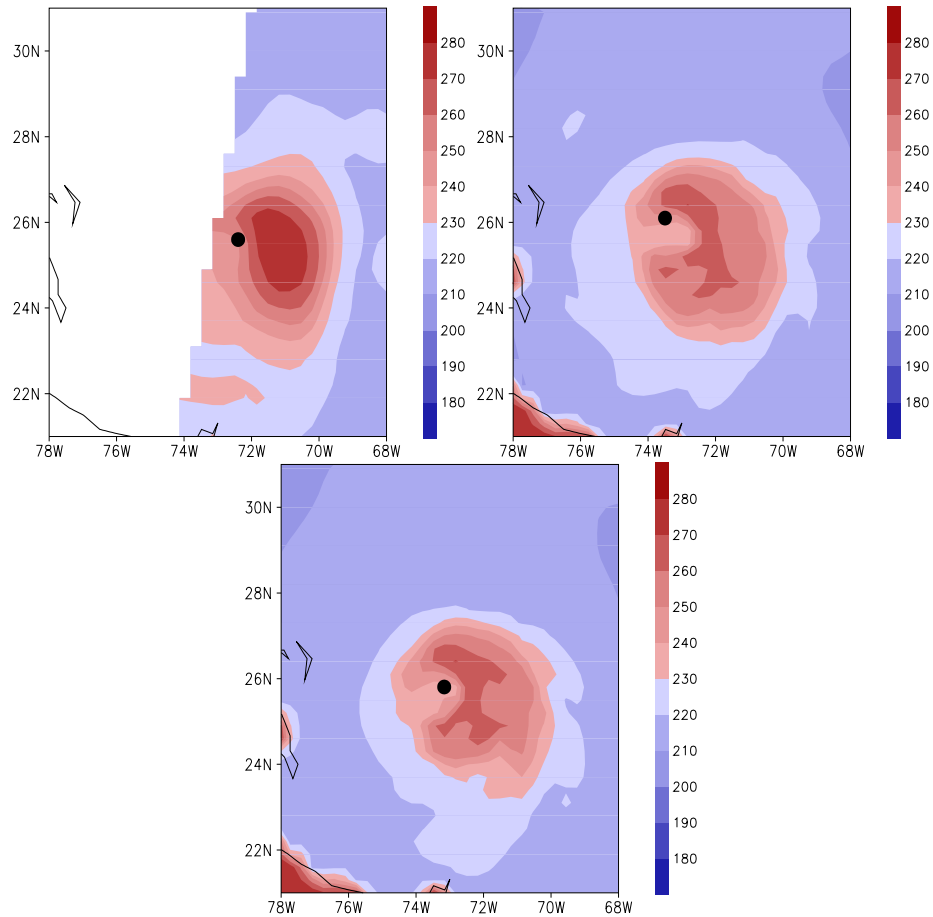


**Figure 5.14.** 19V  $T_b$ s from SSM/I observations (upper left), model-produced from the 24 h ETB forecast (upper right) and the 24 h CNTRL forecast (lower) at 00 UTC 24 August 1998 in units of K. The filled circle represents the observed (upper left) or forecasted (upper right and bottom) center of Hurricane Bonnie.

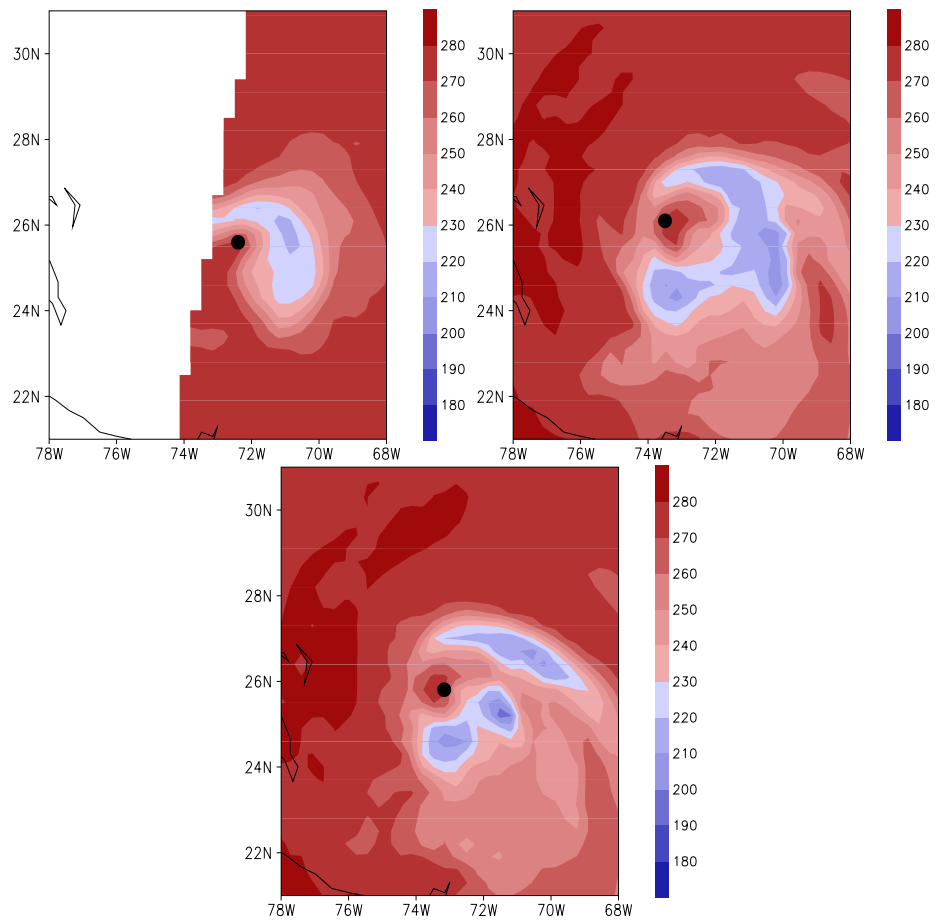


**Figure 5.15.** Same as Figure 5.14 except for 85V  $T_b$ s.

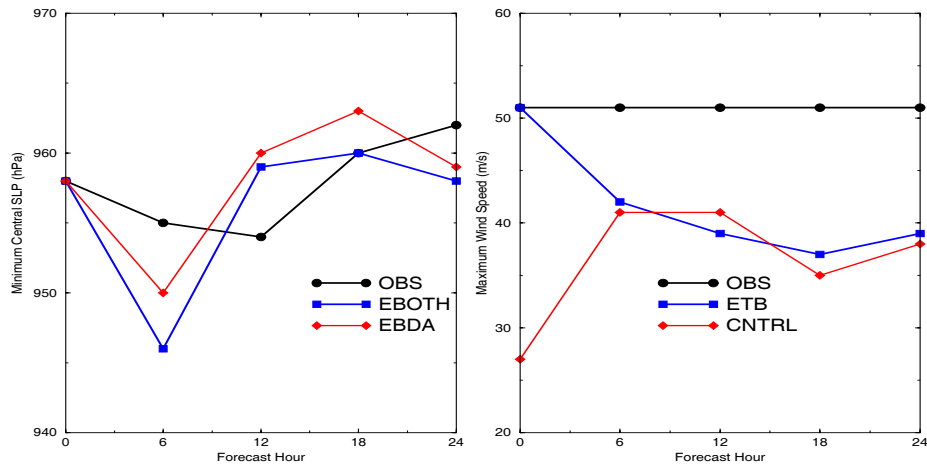


**Figure 5.16.** Observed and forecasted minimum central SLP (left) and maximum surface windspeed (right) from EBOTH and EBDA of Hurricane Bonnie for the 24 h period beginning 1200 UTC 23 August 1998. Units are in hPa (left) and  $\text{m s}^{-1}$ .

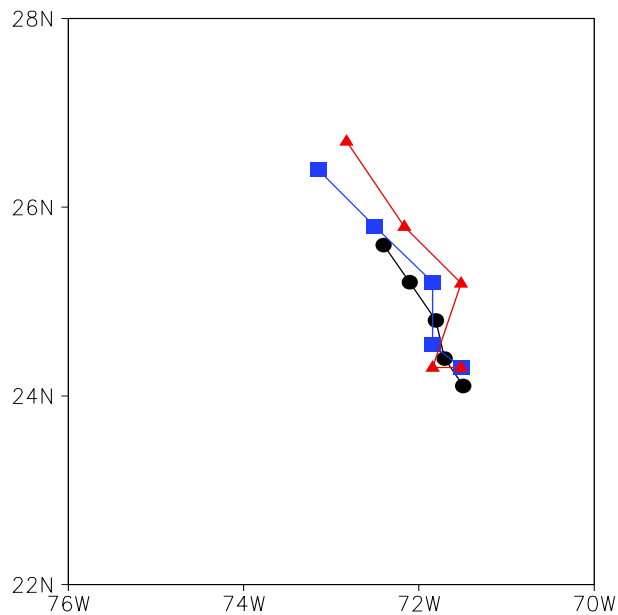


**Figure 5.17.** Observed (black circles) and forecasted track from EBOTH (blue squares) and EBDA (red diamonds) of Hurricane Bonnie for the 24 h period beginning 1200 UTC 23 August 1998.

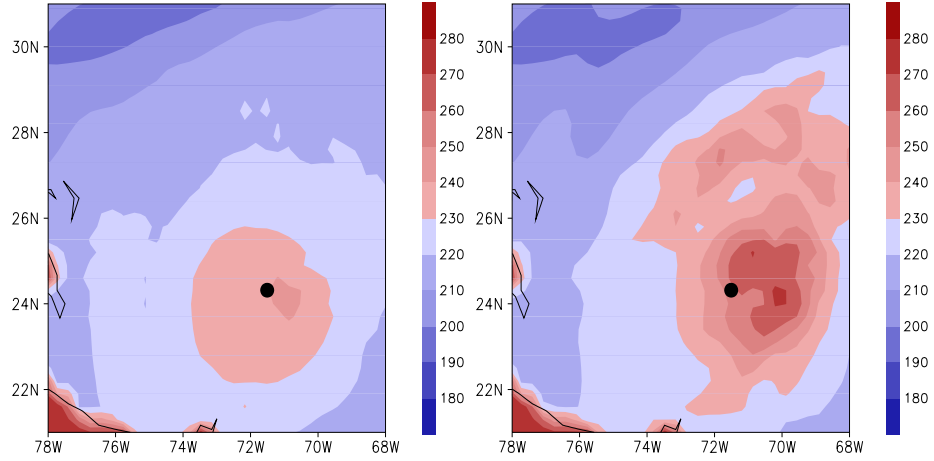


**Figure 5.18.** Model-produced 19V  $T_b$ s from the initial analysis in EBDA (left) and EBOOTH (right) at 12 UTC 23 August 1998 in units of K. The filled circle represents the analyzed center of Hurricane Bonnie.

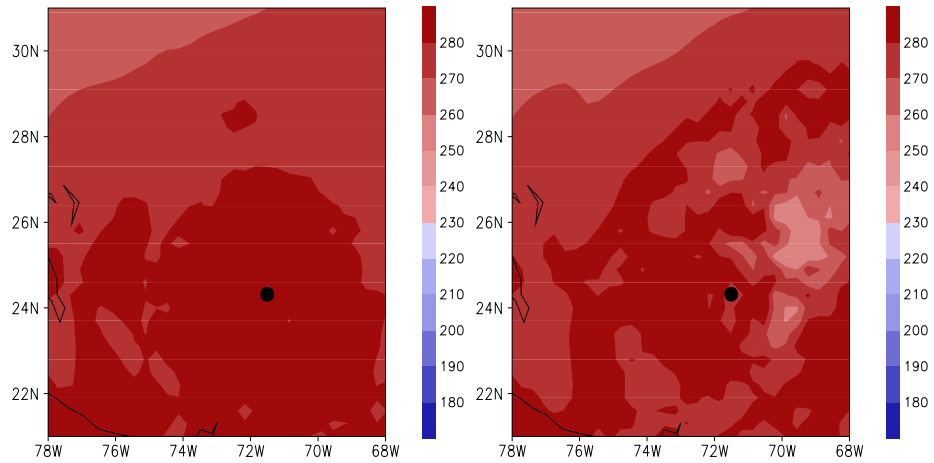


**Figure 5.19.** Same as Figure 5.18 except for the 85V  $T_b$ s.

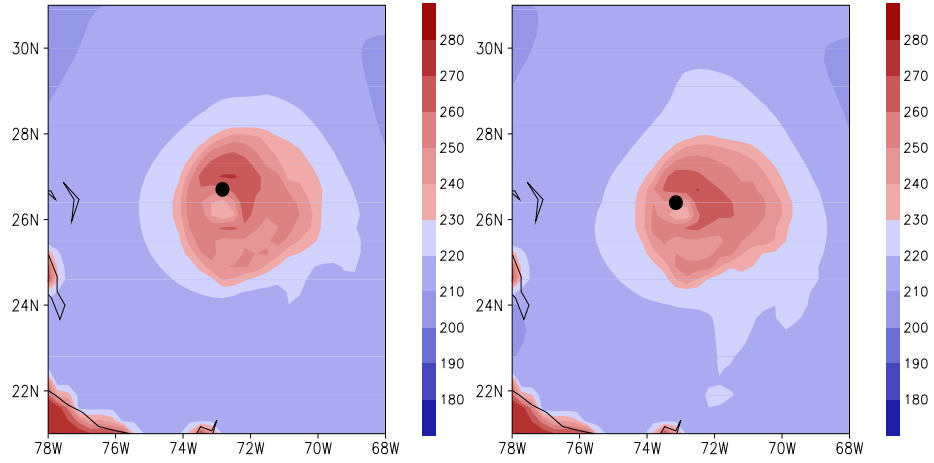


**Figure 5.20.** Same as Figure 5.18 except for 24 h forecast.

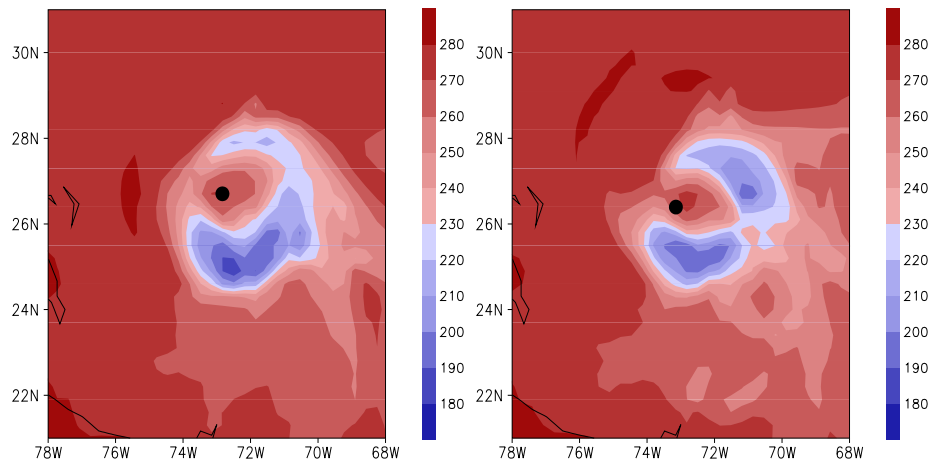


**Figure 5.21.** Same as Figure 5.19 except for 24 h forecast.

## CHAPTER 6

### SUMMARY AND DISCUSSION

This work focused on the development and testing of an adjoint mesoscale modeling system which can be used to assimilate rain-affected observations, such as microwave radiances in tropical cyclone environments. The tangent linear and adjoint models of the COAMPS atmospheric model were written using a combination of manual coding and automatic code generation. The tangent linear and adjoint boundary layer TKE, cumulus, and explicit moist physics parameterizations are included in the system. The code has been structured for distributed memory environments so that it can be run in parallel. The assimilation scheme includes a quasi-Newton LBFGS minimization scheme that uses the gradient calculated by the adjoint model to reduce the value of a scalar cost function which measures the misfit between the COAMPS model state vector and observations. The model state vector includes hydrometeor values so that information on the precipitation fields can be added to the analysis.

A number of test were conducted on the tangent linear and adjoint codes. The tangent linear approximation does not hold as well when the cumulus and explicit moisture schemes are included in the model integrations because of the discontinuities present in these schemes. However, a series of twin minimization experiments show that a suitable amount of decrease in the cost function can be obtained in all model variables (including the hydrometeor values) even with the moisture schemes included in the model runs. More tests are needed to see what type of improvement can be expected using grids with resolutions on the the cloud scale (1-10 km) for which the explicit moisture scheme was designed to work best.

Next, we looked at the ability of an RTM to compute realistic  $T_b$ s in areas of precipitation. The RTM was updated to include the Garnett-Maxwell mixing formula which improved the model's results when compared to observations in areas of high frozen hydrometeor concentrations. PDFs of model-produced and observed  $T_b$ s showed that overall, the model

matches the observations, although the model is producing more areas of precipitation. These results are similar to the results of Chevallier and Bauer [24].

Estimates of the background error for the hydrometeor fields needed in the assimilation process were also investigated. Vertical background error covariance matrices were calculated using the differences between model forecasts which utilized different explicit moisture schemes. The statistics of these differences were assumed to be a reliable estimate of the statistics of the estimate of the error in the background field. SVD was used to recalculate these matrices using only the largest singular value. This process removed the noise in the inverse matrices while retaining most of the information in the background error covariance matrices.

Finally, we looked at the impact that the assimilation of SSM/I  $T_b$ s has on hurricane analyses and prediction. The model-produced  $T_b$ s calculated from the analysis after the assimilation procedure match the observations well for the lower frequency channels (19, 22, and 37 GHz) which are sensitive to water vapor and liquid precipitation. However, for the 85 GHz channel, the analysis  $T_b$ s are roughly 20 K higher than the observations in areas of heavy precipitation. The assimilation of  $T_b$ s increased the maximum surface windspeed in the analysis to a value close to the observation, but a synthetic SLP field also needed to be assimilated in order to see improvement in the the analyzed value of the minimum central SLP. The model was unable to sustain the high windspeeds produced by the  $T_b$  assimilation, but the forecasted strength of the hurricane was slightly stronger after the assimilation of  $T_b$ s. The model was also unable to sustain the initial hydrometeor fields produced by the assimilation process; therefore, it was difficult to conclude what impact the assimilation of  $T_b$ s had on the forecast in radiance space. In future experiments, longer assimilation windows will be incorporated in an attempt to create an initial state that retains more of the information in the analysis during the early forecast periods.

Further work is required to maximize the benefit of these observations on hurricane forecasts. More observations, especially those which give information on variables important to the dynamical structure of the storm may be required in order to improve the intensity and track forecasts. Increasing the grid resolution may also improve the assimilation results and hurricane forecasts, especially since the explicit moisture scheme was designed for smaller grid scales. Increasing the model's resolution will also allow us to turn off the cumulus

parameterization and may lead to a better representation of the frozen hydrometeor fields when the convection is explicitly modeled. Nevertheless, the usefulness of the COAMPS-AMS has been demonstrated in assimilating observations affected by precipitation, which will hopefully lead to further study and improvement of precipitation fields in analyses and forecasts.

## APPENDIX

### LIST OF ACRONYMS

- 1D-Var - One dimensional variational
- 4D-Var - Four dimensional variational
- BDA - Bogus Data Assimilation
- COAMPS - Coupled Ocean Atmosphere Mesoscale Prediction System
- COAMPS - COAMPS Adjoint Modeling System
- DMSP - Defense Meteorological Satellite Program
- LBFGS - Limited Memory Broyden Fletcher Goldfarb Shanno
- MM5 - Fifth Generation Penn State / NCAR Mesoscale Model
- MPI - Message Passing Interface
- MVOI - Multivariate Optimal Interpolation
- NCAR - National Center for Atmospheric Research
- NMC - National Meteorological Center
- NOGAPS - Navy Operational Global Atmospheric Prediction System
- NRL - Naval Research Laboratory
- PDF - Probability Density Function
- RTM - Radiative Transfer Model

- SLP - Sea Level Pressure
- SSM/I - Special Sensor Microwave Imager
- SVD - Singular Value Decomposition
- TAMC - Tangent Linear and Adjoint Model Compiler
- TKE - Turbulent Kinetic Energy

## REFERENCES

- [1] F. Le Dimet and O. Talagrand. Variational algorithms for analysis and assimilation of meteorological observations: Theroretical aspects. *Tellus*, 38A:97–110, 1986.
- [2] J. Lewis and J. Derber. The use of adjoint equations to solve a variational adjustment problem with advective constraints. *Tellus*, 37A:309–322, 1985.
- [3] I. M. Navon, X. Zou, J. Derber, and J. Sela. Variational data assimilation with an adiabatic version of the NMC spectral model. *Mon. Wea. Rev.*, 120:1433–1466, 1992.
- [4] M. Zupanski. Regional four-dimensional variational data assimilation in a quasi-operational forecasting environment. *Mon. Wea. Rev.*, 121:2396–2408, 1993.
- [5] P. Coutier, J.-N., and A. Hollingsworth. A strategy for operational implmentation of 4d-var using an incrmental approach. *Q. J. R. Meteor. Soc.*, 124:1738–1808, 1994.
- [6] X. Zou, F. Vandenberghe, M. De Pondecas, and Y.-H. Kuo. Introduction to adjoint techniques and the MM5 adjoint modeling system. Technical Report NCAR/TN-435-STR, NCAR, 1997.
- [7] F. Rabier, H. Jarvinen, E. Klinker, J.-F. Mahfouf, and A. Simmons. The ECMWF operational implmentation of four-dimensional variational assimilation. I: Experimental results with simplified physics. *Q. J. R. Meteor. Soc.*, 126A:1143–1170, 2000.
- [8] X. Zou, Q. Xiao, A. Lipton, and G. Modica. A numerical study of the effect of GOES sounder cloud-cleared brightness temperatures on the prediction of Hurricane Felix. *J. App. Met.*, 40:34–55, 2001.
- [9] S. Park and D. Zupanski. Four-dimensional variational data assimilation for mesoscale and storm-scale applications. *Meteor. Atm. Phy.*, 82:173–208, 2003.
- [10] X. Zou, Y.-H. Kuo, and Y.-R. Guo. Assimilation of atmospheric radio refractivity using a nonhydrostatic adjoint model. *Mon. Wea. Rev.*, 123:2229–2249, 1995.
- [11] X. Zou and Y.-H. Kuo. Rainfall assimilation through an optimal control of initial and boundary conditions in a limited-area mesoscale model. *Mon. Wea. Rev.*, 124:2859–2882, 1996.
- [12] J. Sun and N. Crook. Dynamical and microphysical retrieval from doppler radar observations using a cloud model and it adjoint. part I: Model development and simulated data experiments. *J. Atmos. Sci.*, 54:1642–1661, 1997.

- [13] Y.-R. Guo, Y.-H. Kuo, J. Dudhia, D. Parsons, and C. Rocken. Four-dimensional variational data assimilation of heterogenous mesoscale observations for a strong convective case. *Mon. Wea. Rev.*, 128:619–643, 2000.
- [14] X. Zou and Q. Xiao. Studies on the initialization and simulation of a mature hurricane using a variational bogus data assimilation scheme. *J. Atmos. Sci.*, 57:836–860, 2000.
- [15] M. Zupanski, D. Zupanski, D. Parrish, E. Rogers, and G. DiMego. Four-dimensional variational data assimilation for the blizzard of 2000. *Mon. Wea. Rev.*, 130:1967–1988, 2002.
- [16] S.-Q. Peng and X. Zou. Assimilation of NCEP multi-sensor hourly rainfall data using the 4D-Var approach: A case study of the squall line on 5 April 1999. *J. Met. Atm. Phys.*, 81:237–255, 2002.
- [17] T. Vukicevic, T. Greenwald, M. Zupanski, D. Zupanski, T. Vonder Haar, and A. Jones. Mesoscale cloud state estimation from visible and infrared satellite radiances. *Mon. Wea. Rev.*, 132:3066–3077, 2004.
- [18] J. Eyre, G. Kelly, A. McNally, E. Anderson, and A. Persson. Assimilation of TOVS radiance information through one-dimensional variational analysis. *Q. J. R. Met. Soc.*, 119:1427–1463, 1993.
- [19] L. Phalippou. A variational retrieval of humidity profile, wind speed and cloud liquid-water path with the SSM/I: Potential for numerical weather prediction. *Q. J. R. Met. Soc.*, 122:327–355, 1996.
- [20] E. Moreau, P. Bauer, and F. Chevallier. Variational retrieval of rain profiles from spaceborne passive microwave radiance observations. *J. Geo. Res.*, 108 (D16):ACL 11–1–ACL 11–18, 2003.
- [21] E. Moreau, P. Lopez, P. Bauer, A. Tompkins, M. Janiskova, and F. Chevallier. Variational retrieval of temperature and humidity profiles using rain rates versus microwave brightness temperatures. *Q. J. R. Meteorol. Soc.*, 130:827–852, 2004.
- [22] G. Liu. A fast and accurate model for microwave radiance calculations. *J. Met. Soc. Jap.*, 76:335–343, 1986.
- [23] C. Amerault and X. Zou. Preliminary steps in assimilating SSM/I brightness temperatures in a hurricane prediction scheme. *J. Ocean. Atmos. Tech.*, 20:1154–1169, 2003.
- [24] F. Chevallier and P. Bauer. Model rain and clouds over oceans: Comparison with SSM/I observations. *Mon. Wea. Rev.*, 131:1240–1255, 2003.
- [25] A. Hollingsworth and P. Lonnberg. The statistical structure of short-range forecast errors as determined from radiosonde data. part I.: The wind field. *Tellus*, 38A:111–136, 1986.
- [26] P. Lonnberg and A. Hollingsworth. The statistical structure of short-range forecast errors as determined from radiosonde data. part II.: The covariance of height and wind errors. *Tellus*, 38A:137–161, 1986.

- [27] D. Parrish and J. Derber. The National Meteorological Center’s spectral statistical interpolation analysis system. *Mon. Wea. Rev.*, 120:1747–1763, 1992.
- [28] R. Daley and E. Barker. NAVDAS: Formulation and diagnostics. *Mon. Wea. Rev.*, 129:869–883, 2001.
- [29] N. Ingleby. The statistical structure of forecast errors and its representation in the Met Office global 3d variational data assimilation scheme. *Q. J. R. Meteor. Soc.*, 127:209–231, 2001.
- [30] J. Klemp and R. Wilhelmson. The simulation of three-dimensional convective storm dynamics. *J. Atmos. Sci.*, 35:1070–1096, 1978.
- [31] R. Hodur. The Naval Research Laboratory’s coupled ocean/atmosphere mesoscale prediction system (COAMPS). *Mon. Wea. Rev.*, 125:1414–1430, 1997.
- [32] D. Perkey and C. Krietzberg. A time-dependent lateral boundary scheme for limited-area primitive equations models. *Mon. Wea. Rev.*, 104:744–755, 1976.
- [33] C.H. Davies. A lateral boundary formulation for multi-level prediction models. *J. Atmos. Sci.*, 102:405–418, 1976.
- [34] G. Mellor and T. Yamada. A hierarchy of turbulence closure models for planetary boundary layers. *J. Atmos. Sci.*, 31:1791–1806, 1974.
- [35] J. Louis. A parametric model of vertical eddy fluxes in the atmosphere. *Bound.-Layer. Meteor.*, 37:187–202, 1979.
- [36] J. Deardorff. Stratocumulus-capped mixed layers derived from a three-dimensional model. *Bound.-Layer. Meteor.*, 18:495–527, 1980.
- [37] R. Harshvardhan, D. Randall, and T. Corsetti. A fast radiation parameterization for atmospheric circulation models. *J. Geophys. Res.*, 92:40–63, 1997.
- [38] J. Kain and J. Fritsch. Convective parameterization for mesoscale models: The Kain-Fritsch scheme. In *The Representation of Cumulus Convection in Numerical Models, Meteorological Monographs*, volume 46, pages 165–170. American Meteorological Society, 1993.
- [39] H. Kuo. On formation and intensification of tropical cyclones through latent heat release by cumulus convection. *J. Atmos. Sci.*, 22:40–63, 1965.
- [40] S. Rutledge and P. Hobbs. The mesoscale and microscale structure of organization of clouds and precipitation in midlatitude cyclones. VIII: A model for the seeder-feeder process in warm-frontal rainbands. *J. Atmos. Sci.*, 40:1185–1206, 1983.
- [41] S. Rutledge and P. Hobbs. The mesoscale and microscale structure of organization of clouds and precipitation in midlatitude cyclones. XII: A diagnostic modeling study of precipitation development in narrow cold-frontal bands. *J. Atmos. Sci.*, 41:2949–2972, 1984.

- [42] M. Khairoutdinov and Y. Kogan. A new cloud physics parameterization in a large-eddy simulation model of marine stratocumulus. *Mon. Wea. Rev.*, 128:229–243, 2000.
- [43] J. Marshall and W. Palmer. The distribution of raindrops with size. *J. Meteor.*, 5:165–166, 1948.
- [44] A. Lorenc. Analysis methods for numerical weather prediction. *Q. J. R. Meteor. Soc.*, 112:1177–1194, 1986.
- [45] R. Giering and T. Kaminski. Recipes for adjoint code construction. *ACM Trans. On Math. Software*, 24:437–474, 1998.
- [46] X. Zou. Tangent linear and adjoint of “on-off” processes and their feasibility for use in 4-dimensional variational data assimilation. *Tellus*, 49A:3–31, 1997.
- [47] S. Zhang, X. Zou, and J. Ahlquist. Examination of numerical results from tangent linear and adjoint of discontinuous nonlinear models. *Mon. Wea. Rev.*, 129:2791–2804, 2001.
- [48] D. Liu and J. Nocedal. On the limited memory BFGS method for large-scale optimization. *Math Program.*, 45:503–528, 1989.
- [49] P. Wolfe. The secant method for simultaneous nonlinear equations. *Comm. ACM*, 2:12–13, 1968.
- [50] M. Zupanski. A preconditioning algorithm for large-scale minimization problems. *Tellus*, 45A:478–492, 1993.
- [51] M. Zupanski. A preconditioning algorithm for four-dimensional variational data assimilation. *Mon. Wea. Rev.*, 124:2562–2573, 1996.
- [52] J. Dudhia. A nonhydrostatic version of the Penn State-NCAR mesoscale model: Validation tests and simulation of an Atlantic cyclone and cold front. *Mon. Wea. Rev.*, 121:1493–1513, 1993.
- [53] J. Reisner, R. Rasmussen J., and R. Bruintjes. Explicit forecasting of supercooled liquid water in winter storms using the MM5 mesoscale model. *Q. J. R. Meteorol. Soc.*, 124:1071–1107, 1998.
- [54] W.-K. Tao and J. Simpson. A further study of cumulus interaction and mergers: Three-dimensional simulations with trajectory analyses. *J. Atmos. Sci.*, 46:2974–3004, 1989.
- [55] P. Shultz. An explicit cloud physics parameterization for operational numerical weather prediction. *Mon. Wea. Rev.*, 123:3331–3343, 1995.
- [56] Y.-L. Lin, R. Farley, and H. Orville. Bulk parameterization of the snow field in a cloud model. *J. Clim. App. Met.*, 22:1065–1092, 1983.
- [57] J. Hollinger, R. Lo, G. Poe, R. Savage, and J. Pierce. Special sensor microwave/imager user’s guide. Technical report, Naval Research Laboratory, 1987.

- [58] T. Fujita. Pressure distribution within a typhoon. *Geophys. Mag*, 23:437–451, 1952.
- [59] K. Park and X. Zou. Toward developing an objective 4D-Var BDA scheme for hurricane initialization based on TPC observed parameters. *Mon. Wea. Rev.*, 132:2054–2069, 2004.
- [60] K.-N Liou. Analytic two-stream and four-stream solutions for radiative transfer. *J. Atmos. Sci.*, 31:1473–1475, 1974.
- [61] C. Bohren and L. Battan. Radar backscattering by inhomogeneous precipitation particles. *J. Atmos. Sci.*, 37:1821–1827, 1980.
- [62] P. Bauer, A. Khain, A. Pokrovsky, R. Meneghini, C. Kummerow, F. Marzano, and J. Baptista. Combined cloud-microwave radiative transfer modeling of stratiform rain. *J. Atmos. Sci.*, 57:1082–1104, 2000.
- [63] G. Skofronick-Jackson, A. Gasiewski, and J. Wang. Influence of microphysical cloud parameterizations on microwave brightness temperatures. *IEEE. Trans. Geo. Rem. Sens.*, 40:187–196, 2002.
- [64] S. Barnes. A technique for maximizing details in numerical weather maps analysis. *J. Appl. Meteor.*, 3:396–409, 1964.
- [65] K. Aonashi and G. Liu. Direct assimilation of multichannel microwave brightness temperatures and impact on mesoscale numerical weather prediction over the TOGA COARE domain. *J. Met. Soc. Jap.*, 77:771–794, 1999.
- [66] F. Chevallier, P. Bauer, J.-F., Mahfouf, and J.-J. Morcrette. Variational retrieval of cloud liquid profile from ATOVS observations. *Q.J.R. Meteorol. Soc.*, 128:2511–2526, 2002.

## **BIOGRAPHICAL SKETCH**

**Clark Matthew Amerault**

### **Education**

Ph.D. Meteorology, May 2005, The Florida State University, Tallahassee, FL.

M.S. Meteorology, August 2002, The Florida State University, Tallahassee, FL.

B.S. Atmospheric Sciences, January 2000, Cornell University, Ithaca, NY.

### **Experience**

2000-present: Graduate Research Assistant / Department of Meteorology, FSU

2001: Teaching Assistant / Department of Meteorology, FSU

1999: Undergraduate Research Assistant / Cornell Theory Center

1999: Teaching Assistant / Cornell University